

Low-order scaling G_0W_0 by pair atomic density fitting

Arno Förster* and Lucas Visscher

*Theoretical Chemistry, Vrije Universiteit, De Boelelaan 1083, NL-1081 HV, Amsterdam,
The Netherlands*

E-mail: a.t.l.foerster@vu.nl

Abstract

We derive a low-scaling G_0W_0 algorithm for molecules, using pair atomic density fitting (PADF) and a imaginary time representation of the Green's function and describe its implementation in the Slater type orbital (STO) based Amsterdam density functional (ADF) electronic structure code. We demonstrate the scalability of our algorithm on a series of water clusters with up to 432 atoms and 7776 basis functions and observe asymptotic quadratic scaling with realistic threshold qualities controlling distance effects and basis sets of triple- ζ (TZ) plus double polarization quality. Also owing to a very small prefactor, with these settings a G_0W_0 calculation for the largest of these clusters takes only 240 CPU hours. We assess the accuracy of our algorithm for HOMO and LUMO energies in the GW100 database. With errors of 0.24 eV for HOMO and 0.52 eV for LUMO energies on the QZ-level for GW100, our implementation is less accurate than canonical all-electron implementations using GTO-type basis sets. This is related to the well-known shortcomings of the GW space-time method using analytical continuation techniques as well as to numerical issues of the PADF-approach of accurately representing diffuse AO-products. We speculate, that this issue might be overcome by using optimized auxiliary fit sets with more diffuse functions of

higher angular momenta. Despite these shortcomings, for subsets of medium and large molecules from the GW5000 database, the error of our approach using basis sets of TZ and augmented DZ quality is decreasing with system size. On the augmented DZ level we reproduce canonical, complete basis set limit extrapolated reference values with an accuracy of 80 meV on average for a set of 20 large organic molecules. We anticipate our algorithm, in its current form, to be very useful in the study of single-particle properties of large organic systems such as chromophores and acceptor molecules.

1 Introduction

Spectroscopy provides fundamental insights into the optical and electronic properties of matter and thus plays a decisive role in chemistry and material science.^{1–5} The great potential of computational spectroscopy is leveraged increasingly to complement and understand spectroscopic experiments.^{6–15} Still, no existing computational method can be applied routinely to systems of hundreds of atoms and simultaneously predict the outcome of a spectroscopic experiment with satisfactory accuracy.¹⁵ For ground state properties, Kohn-Sham (KS)¹⁶ density functional theory (DFT)^{17–19} has been proven to be very accurate for many weakly correlated molecular systems.^{20–26} Excited particles, however, interact strongly with other electrons and semi-local or hybrid approximations to the exact functional of KS-DFT do not capture this physics correctly.^{27–36} Consequently, they fail to adequately describe single-particle excitations, being necessary to understand and predict phenomena like transport,^{37–39} tunneling,^{40–42} or photoemission.^{43–48}

Many body perturbation theory (MBPT)^{49–51} based on Hedin’s equations describes the correlation of the excited electron with its surrounding by an expansion in powers of the response of the systems total classical potential to an external perturbation.^{52–54} Only taking into account the first-order term of this expansion is called GW-approximation.^{51,55} Accounting for the major part of electron correlation,^{46,54,56,57} it makes MBPT computationally tractable, greatly improves over DFT for the description of single-particle excitations^{46,53,58}

and also paves the way toward accurate optical spectra using the Bethe-Salpeter equation formalism.^{59,60} Large numbers of computational material science codes^{48,56,61–72} feature GW implementations and also in the quantum chemistry community it has acquired some momentum over the last years.^{58,73–93}

The downside of the GW method is its huge operation count compared to KS-DFT, preventing its routine application to large systems. A popular approach to reduce the prefactor, frequently outperforming self-consistent approaches for charged excitations,^{58,94} is the so-called G_0W_0 -approximation in which the self-energy is calculated using a mean-field Green's function. Still, the operation count of a G_0W_0 calculation increases as N^4 as a function⁹⁵ of system size N and compared to KS-DFT, GW quasi-particle (QP) energies converge significantly slower with the size of the single-particle basis.^{46,96,97} Consequently, the last years have witnessed some effort to reduce time-to-solution further which resulted in massively parallel implementations optimized for state-of-the-art supercomputers^{98,99} but also in notable algorithmic developments, including stochastic approaches,^{100–102} implementations avoiding the explicit summation over empty electronic states in the polarizability, P ^{103–106} low-rank approximations to the dielectric function ϵ ^{64,97,107} or the screened interaction W ,^{108,109} and basis set error (BSE) correction schemes.^{110–112}

In *ab initio* calculations on molecular systems, atom centered localized atomic orbitals (AO) are commonly employed¹¹³ In this representation, the dimensions of W and P grow as N^2 , making the evaluation of W an N^6 operation. One can employ an implicit low-rank approximation to both quantities by transforming them to a smaller auxiliary basis. Such transformations, most importantly density fitting (DF)^{114–126} and Cholesky decomposition (CD)^{127–131} techniques, are employed in quantum chemistry since nearly half a century^{114–116} and they are routinely used in GW implementations for molecules^{70,132–139} where their accuracy is well documented.^{82,135} Using these techniques, the evaluation of W becomes an N^3 -operation with a sufficiently small prefactor. However, the transformations from product basis to auxiliary basis and back, usually implicit in the evaluation of P and the self-energy

Σ , respectively, still scale as N^4 .

This issue can in principle be avoided by constructing a sparse transformation matrix using local DF approximations (LDF).^{140–143} However, conventional GW calculations are performed in frequency space, necessitating a representation of the Green's function in the MO basis where the sparsity of the transformation matrix is lost. From this perspective, the Green's function is more conveniently represented in imaginary time^{29,144–148} since the energy denominator in P factorizes and the relevant equations can be transformed to the AO basis where LDF might be used efficiently.

LDF techniques have originally been proposed to evaluate the Fock matrix in generalized KS (gKS)- and Hartree-Fock (HF) calculations in a low-scaling fashion.¹¹⁵ This is fortunate, since in imaginary time the evaluation of Σ is equivalent to calculating the exact exchange contribution to the Fock matrix. In the most extreme LDF-variant, each AO-pair product is expanded in a set of auxiliary basis functions (ABF) centered on the same two atoms as the target pair of primitives. We refer to this approach as pair atomic DF (PADF) and note, that also the names concentric DF, pair-atomic resolution of the identity (PARI), and RI-LVL are encountered in the literature. It has been introduced by Baerends et al. in the 70s,¹¹⁵ and subsequently employed in pure¹⁴⁹ and hybrid^{140,150} DFT calculations. As an efficient way to construct the Fock matrix, it has received renewed attention over the last years^{151–157} and its strengths and shortcomings for this task have been analyzed in detail.^{158,159} It has also been applied to correlated methods and shown to be very accurate when appropriate auxiliary fit sets are used.^{160–163}

For the GW space-time approach¹⁴⁷ to be useful in practice, small grids not only in imaginary time but also in imaginary frequency as well as an efficient way to switch between both domains are needed to avoid potentially prohibitive prefactors and storage bottlenecks. How to address these technical issues has been shown by Kresse and coworkers^{164,165} who subsequently presented cubic scaling GW implementations for periodic systems^{166,167} and also low-scaling space-time RPA^{168,169} and GW⁹⁹ implementations for molecular systems

could be realized in the last years.

It has already been anticipated¹⁶⁰ that PADF is especially well suited to implement GW in a low-scaling fashion. Against this background, we herein derive a GW space-time algorithm whose asymptotic cost associated with the calculation of P and Σ is reduced to N^3 independent of system size, and to N^2 , when distance effects are exploited. We only discuss our G_0W_0 -implementation here while self-consistent GW will be discussed in a future publication. However, we stress that within the herein presented framework quasi-particle^{170,171} and fully self-consistent GW is readily implemented as we always evaluate the complete self-energy matrix instead of only its diagonal in the MO basis.

We implemented our algorithm in the Slater type orbitals (STO) based Amsterdam density functional package (ADF).^{172,173} Thus, our work is the first production level implementation of a GW method using STOs. While we do not aim at a comparison of different types of localized basis functions, we consider our implementation as a necessary first step towards a better understanding of the possible benefits of STOs in MBPT and also as a demonstration that they can be used efficiently in GW calculations. We also emphasize that the herein presented formalism is independent of the actual choice of basis functions, provided that they are local. We already note at this point that similar ideas have been presented by Wilhelm et al.⁹⁹ and implemented in the CP2K package.⁴⁸ We will start the following discussion in section 2 by defining the basic quantities in real space (RS) and imaginary time, discretize them using an AO basis and imaginary time grids and transform them to an auxiliary basis. From this starting point, we outline our algorithm and its implementation before we investigate its accuracy and computational efficiency in section 3. Finally, section 4 concludes this work with a summary and perspectives on further research.

2 Theory

2.1 G_0W_0 in real space and imaginary time

We start this section by briefly outlining the G_0W_0 approximation to Hedin's equations in the random phase approximation (RPA).⁵³ Using the molecular orbitals ϕ_n and corresponding orbital energies ϵ_n obtained from solving

$$[h^{(0)}(\mathbf{r}) - \epsilon_n] \phi_n(\mathbf{r}) + \int_{\mathbb{R}^3} d\mathbf{r}' V_{xc}(\mathbf{r}, \mathbf{r}') \phi_n(\mathbf{r}') = 0 , \quad (1)$$

with a single-particle Hamiltonian $h^{(0)}$ and a potentially local exchange-correlation (xc) potential V_{xc} , the irreducible single-particle time-ordered Green's function in imaginary time is given as

$$G(\mathbf{r}, \mathbf{r}', i\tau) = \Theta(\tau) \underline{G}(\mathbf{r}, \mathbf{r}', i\tau) - \Theta(-\tau) \overline{G}(\mathbf{r}, \mathbf{r}', i\tau) , \quad (2)$$

with

$$\begin{aligned} \underline{G}(\mathbf{r}, \mathbf{r}', i\tau) &= i \sum_i^{occ} \phi_i(\mathbf{r}) \phi_i^*(\mathbf{r}') e^{-|\epsilon_i - \epsilon_F|\tau} , \\ \overline{G}(\mathbf{r}, \mathbf{r}', i\tau) &= i \sum_a^{virt} \phi_a(\mathbf{r}) \phi_a^*(\mathbf{r}') e^{|\epsilon_a - \epsilon_F|\tau} \end{aligned} \quad (3)$$

being particle and hole Green's functions, respectively, i, j, \dots (a, b, \dots) labeling occupied (virtual) orbitals, ϵ_F being the Fermi energy and Θ being the Heavyside step function. The independent-particle polarizability P in the RPA is defined as

$$P(\mathbf{r}, \mathbf{r}', i\tau) = -iG(\mathbf{r}, \mathbf{r}', i\tau)G(\mathbf{r}', \mathbf{r}, -i\tau) , \quad (4)$$

and using (2) and (3) can be written as

$$P(\mathbf{r}, \mathbf{r}', i\tau) = -i \sum_i^{occ} \sum_a^{virt} \phi_i(\mathbf{r}) \phi_i^*(\mathbf{r}') \phi_a(\mathbf{r}') \phi_a^*(\mathbf{r}) e^{-|\epsilon_a - \epsilon_F|\tau} e^{-|\epsilon_i - \epsilon_F|\tau} . \quad (5)$$

The polarizability is the kernel of a Dyson equation relating the reducible (or screened) Coulomb interaction $W(\mathbf{r}, \mathbf{r}', i\tau)$ to the bare Coulomb potential $V(\mathbf{r}, \mathbf{r}') = V'(\mathbf{r}, \mathbf{r}', i\tau)\delta(\tau - \tau')$ (see e.g. ref. 174),

$$W(\mathbf{r}, \mathbf{r}', i\tau) = V(\mathbf{r}, \mathbf{r}') + \int d\tau' d\mathbf{r}_3 d\mathbf{r}_4 V(\mathbf{r}, \mathbf{r}_3) P(\mathbf{r}_3, \mathbf{r}_4, i\tau - i\tau') W(\mathbf{r}_4, \mathbf{r}', i\tau') , \quad (6)$$

which takes the simpler form¹⁴⁸

$$W^{-1}(\mathbf{r}, \mathbf{r}', i\omega) = V^{-1}(\mathbf{r}, \mathbf{r}') - P(\mathbf{r}, \mathbf{r}', i\omega) \quad (7)$$

in the imaginary frequency domain. From this quantity, the irreducible self-energy Σ can be constructed⁵³ which is most conveniently split into a static and a dynamic contribution, $\Sigma = \Sigma^x + \Sigma^c$. The former is the HF exchange kernel and is given as

$$\Sigma^x(\mathbf{r}, \mathbf{r}') = i\underline{G}(\mathbf{r}, \mathbf{r}', i\tau = 0) V(\mathbf{r}, \mathbf{r}') , \quad (8)$$

and the latter as

$$\Sigma^c(\mathbf{r}, \mathbf{r}', i\tau) = iG(\mathbf{r}, \mathbf{r}', i\tau) \widetilde{W}(\mathbf{r}, \mathbf{r}', i\tau) , \quad (9)$$

where we have introduced $\widetilde{W} = W - V$. In a self-consistent procedure, G would be updated by solving another Dyson equation containing Σ as its kernel. In a G_0W_0 calculation, Σ^c is transformed to the imaginary frequency axis from where it is analytically continued to the complex plane.^{175,176} The QP energy ϵ_n^{QS} is the ω which fulfills

$$0 = \omega - \epsilon_n - \langle n | \text{Re}(\Sigma^c(\omega)) + \Sigma_x - V_{xc} | n \rangle , \quad (10)$$

where $\langle n | O | m \rangle$ denote matrix elements of an operator O in the molecular orbital basis.

2.2 G_0W_0 in a local basis

Discretization of real space Assuming we have represented imaginary time and frequency dependence of all quantities through suitable grids, we use (real) STOs χ to discretize RS, so that

$$\phi_n(\mathbf{r}) = \sum_{\mu} b_{\mu n} \chi_{\mu}(\mathbf{r}) . \quad (11)$$

Inserting this definition into eqs. (2) and (3) gives

$$\underline{G}(\mathbf{r}, \mathbf{r}', i\tau) = \sum_i \sum_{\mu\nu} \chi_{\mu}(\mathbf{r}) b_{\mu i} e^{-|\epsilon_i - \epsilon_F| \tau} b_{i\nu} \chi_{\nu}(\mathbf{r}') \quad (12)$$

$$\overline{G}(\mathbf{r}, \mathbf{r}', i\tau) = \sum_a \sum_{\mu\nu} \chi_{\mu}(\mathbf{r}) b_{\mu a} e^{|\epsilon_a - \epsilon_F| \tau} b_{a\nu} \chi_{\nu}(\mathbf{r}') \quad (13)$$

and from the identity

$$G(\mathbf{r}, \mathbf{r}', i\tau) = \sum_{\mu\nu} \chi_{\mu}(\mathbf{r}) G_{\mu\nu, \tau} \chi_{\nu}(\mathbf{r}') \quad (14)$$

we obtain the representation of particle and hole Green's function in the STO basis,

$$G_{\mu\nu, \tau} = \sum_i b_{\mu i} e^{-|\epsilon_i - \epsilon_F| \tau} b_{i\nu} \quad (15)$$

$$\overline{G}_{\mu\nu, \tau} = \sum_a b_{\mu a} e^{|\epsilon_a - \epsilon_F| \tau} b_{a\nu} , \quad (16)$$

which for each discrete $i\tau$ can be seen as an energy-weighted density matrix.¹⁷⁷ While Σ also transforms as a 2-point correlation function,

$$\Sigma_{\mu\nu, \tau} = \int d\mathbf{r} d\mathbf{r}' \chi_{\mu}(\mathbf{r}) \Sigma(\mathbf{r}, \mathbf{r}', i\tau) \chi_{\nu}(\mathbf{r}') , \quad (17)$$

all 2-electron operators transform as 4-point correlation functions,¹⁷⁸

$$P_{\mu\nu\kappa\lambda,\tau} = i\underline{G}_{\mu\nu,\tau} \overline{G}_{\kappa\lambda,\tau} \quad (18)$$

$$V_{\mu\nu\kappa\lambda} = \int d\mathbf{r} d\mathbf{r}' \chi_\mu(\mathbf{r}) \chi_\nu(\mathbf{r}) V(\mathbf{r}, \mathbf{r}') \chi_\kappa(\mathbf{r}') \chi_\lambda(\mathbf{r}') \quad (19)$$

$$\widetilde{W}_{\mu\nu\kappa\lambda,\tau} = \int d\mathbf{r} d\mathbf{r}' \chi_\mu(\mathbf{r}) \chi_\nu(\mathbf{r}) \widetilde{W}(\mathbf{r}, \mathbf{r}', i\tau) \chi_\kappa(\mathbf{r}') \chi_\lambda(\mathbf{r}') . \quad (20)$$

While in this representation P is simply given as a Kronecker product, the calculation of the screened interaction (20) from P and V requires the inversion of a matrix in the AO-product space $\mathcal{P} = \{\chi_\mu\} \otimes \{\chi_\nu\}$ for all frequency points (either of W^{-1} as in (7) or of the dielectric function ϵ which is calculated from P and V) whose dimension scales as N^2 with system size. Hence, the matrix inversion scales as N^6 .

This scaling does not reflect the systems physics and is simply an artefact of the chosen representation. The Eckard–Young theorem guarantees the optimal rank- r approximation $M^{(r)}$ to some matrix M to be given by the first r terms in the sum on the *r.h.s.* of

$$M^{(r)} = \sum_i^r \sigma_i v_i \otimes u_i, \quad \sigma_i \geq \sigma_{i+1} , \quad (21)$$

where σ is a singular value and v_i and u_i are vectors of the matrices V and U from the singular value decomposition (SVD) of M . In this way one can indeed show that the ranks of P , V and W should only grow linearly with system size¹⁷⁹ and using (21) one might decompose P , V and W (given that they are symmetric) as

$$M_{\mu\nu\kappa\lambda} = \sum_{pq} C_{\mu\nu p} Z_{pq} [C^T]_{q\kappa\lambda}, \quad M = P, V, \widetilde{W} , \quad (22)$$

where Z is the diagonal matrix of singular values and C collects the left singular vectors of M . An explicit SVD would scale as $N_{AO}^4 r$ and is prohibitive in practice.¹⁷⁹ Instead, it is common practice to represent V and W in a predefined auxiliary basis $\mathcal{A} = \{f\}$, growing

linearly with system size. Expanding all AO-pair products in terms of \mathcal{A} ,

$$\chi_\mu(\mathbf{r})\chi_\nu(\mathbf{r}) = \sum_p C_{\mu\nu p} f_p(\mathbf{r}) , \quad (23)$$

where Greek lowercase letters label AOs and the Roman lowercase letters p, q, \dots refer to ABFs, V and \widetilde{W} can be expressed as

$$V_{pq} = \int d\mathbf{r} d\mathbf{r}' f_p(\mathbf{r}) V(\mathbf{r}, \mathbf{r}') f_q(\mathbf{r}') \quad (24)$$

$$\widetilde{W}_{pq} = \int d\mathbf{r} d\mathbf{r}' f_p(\mathbf{r}) \widetilde{W}(\mathbf{r}, \mathbf{r}') f_q(\mathbf{r}') , \quad (25)$$

and with (22) and (23), the equations to be solved in a G_0W_0 calculation become

$$P_{pq,\tau} = C_{\mu\nu p} P_{\mu\nu\kappa\lambda,\tau} C_{\kappa\lambda q} = -i C_{\mu\nu p} \underline{G}_{\mu\kappa,\tau} \overline{G}_{\nu\lambda,\tau} C_{\kappa\lambda q} \quad (26)$$

$$W_{pq,\omega} = V_{pq} + V_{pr} P_{rs,\omega} W_{sq,\omega} = [V^{-1} - P]_{pq,\omega}^{-1} \quad (27)$$

$$\Sigma_{\mu\nu}^x = i \sum_{\kappa\lambda} \sum_{pq} \underline{G}_{\kappa\lambda,\tau=0} C_{\mu\kappa q} V_{pq} C_{\nu\lambda p} \quad (28)$$

$$\Sigma_{\mu\nu,\tau}^c = i \sum_{\kappa\lambda} \sum_{pq} G_{\kappa\lambda,\tau} C_{\mu\kappa q} \widetilde{W}_{pq,\tau} C_{\nu\lambda q} , \quad (29)$$

replacing eqs. (5) and (7)–(9). In this set of equations, (26) is the computational bottleneck. While the basis transformation in the first equation in (26) would scale as N^5 , also using the second equation one ends up with a scaling of N^4 . The same is actually true for (8) and (9), however, as in a G_0W_0 calculation only the diagonal elements of Σ in the MO basis are needed, the computational effort reduces to N^3 .

Improvements over the N^4 -scaling can be achieved in essentially two ways. The first way relies on the asymptotically exponential decay of the density matrix.^{180–182} Ochsenfeld and coworkers exploited the resulting sparsity in \underline{G} and \overline{G} ¹⁸³ to calculate correlation energies in second order Møller–Plesset perturbation theory (MP2)^{184–186} and RPA.^{187–190} It is an obvious drawback of the approach that in 3D systems the density matrix is less sparse as

one would hope for,^{191–193} especially for large AO basis sets with many diffuse functions commonly employed in GW calculations. The second way is to construct a sparse map from \mathcal{P} to \mathcal{A} . How this can be achieved will be discussed in the next paragraph.

Local density fitting approximations Given some target precision ϵ , the two main goals of DF are first, to find a matrix M' with dimension N_{aux} for which

$$\|M - M'\| < \epsilon \quad (30)$$

with N_{aux} as small as possible and M defined by (22) and second, to improve over the unfavourable scaling of eqs. (26), (28) and (29) by constructing C in a way that it becomes sparse. Both goals are in principle in conflict with each other. In DF, one minimizes the residual function

$$r_{\mu\nu}(\mathbf{r}) = \chi_\mu(\mathbf{r})\chi_\nu(\mathbf{r}) - \sum_p C_{\mu\nu p} f_p(\mathbf{r}) \quad \forall \mu, \nu, \quad (31)$$

with respect to some appropriate norm. In the RI-V approach, the Coulomb repulsion of r is minimized,

$$\frac{\partial}{\partial C_{\kappa\lambda q}} \int d\mathbf{r} d\mathbf{r}' r_{\kappa\lambda}(\mathbf{r}) V(\mathbf{r}, \mathbf{r}') r_{\mu\nu}(\mathbf{r}') = 0, \quad (32)$$

and it follows that

$$\sum_p C_{\mu\nu p} V_{pq} = \int d\mathbf{r} d\mathbf{r}' \chi_\mu(\mathbf{r})\chi_\nu(\mathbf{r}) V(\mathbf{r}, \mathbf{r}') f_q(\mathbf{r}'), \quad (33)$$

i.e. the error in the low-rank approximation of V is quadratic in r since the terms linear in C vanish. Of course, a similar conclusion can not be drawn for P and consequently also not for W . Still, it seems that this metric is an excellent choice if the goal is to fulfil (30) with N_{aux} as small as possible and using auxiliary fit sets from standard libraries. As shown by van Setten et al, QP HOMOs and LUMOs only deviate by a few meV from the ones obtained from calculations without any low-rank approximation^{82,135} when appropriate auxiliary fit

sets^{125,194} are used.

On the other hand, RI-V is a very bad choice in the sense that the slow decay of the kernel of the Coulomb operator ensures that C will be dense. In the RI-SVS approach,^{118,121} (31) is minimized with respect to the L_2 norm which requires larger N_{aux} to fulfil (30) but results in a C with the number of non-zero elements increasing only linearly with system size for exponentially decaying basis functions. It has been shown by Wilhelm et al. that this approach results in tremendous speed-ups in the evaluation of eqs. (26), (28) and (29) without requiring to large N_{aux} to make the evaluation of (27) problematic for systems of more than 1000 atoms.⁹⁹ However, for rather small systems with a 3D structure, the number of non-zero elements in C will not be much different from $N_{AO}^2 \times N_{aux}$. Thus, due to the usually larger N_{aux} compared to RI-V, the method will only be advantageous for sufficiently large systems.⁹⁹

In LDF approximations, this shortcoming is addressed by building in sparsity into the fitting procedure *a priori*. In PADF, an expansion of the pair-density $\chi_\mu(\mathbf{r})\chi_\nu(\mathbf{r})$ of the form

$$\chi_\mu(\mathbf{r})\chi_\nu(\mathbf{r}) = \sum_{p \in A \cup B} C_{\mu\nu p} f_p(\mathbf{r}) \quad \forall \mu \in A, \nu \in B \quad (34)$$

is employed so that the number of non-zero elements in C scales at most quadratic with system size. In our implementation, we also define thresholds $d_{\mu\nu}$ for each AO-product and assume $C_{\mu\nu p} = 0$ if $|\mathbf{R}_A - \mathbf{R}_B| > d_{\mu\nu}$ so that the number of non-zero elements in C only increases linearly.¹⁶² For each atom, we also reorder all AOs from the most diffuse to the least diffuse one so that all non-zero elements in C are grouped in dense blocks. Eq. (31) becomes

$$r_{\mu\nu}^{PADF}(\mathbf{r}) = \chi_\mu(\mathbf{r})\chi_\nu(\mathbf{r}) - \sum_{p \in A \cup B} C_{\mu\nu p} f_p(\mathbf{r}) \quad \forall \mu \in A, \nu \in B , \quad (35)$$

which is minimized with respect to the Coulomb metric. Solving

$$\frac{\partial}{\partial C_{\kappa\lambda q}} \int d\mathbf{r} d\mathbf{r}' r_{\kappa\lambda}^{PADF}(\mathbf{r}) V(\mathbf{r}, \mathbf{r}') r_{\mu\nu}^{PADF}(\mathbf{r}') = 0 , \quad (36)$$

does not lead to an equation of the form (33) as the terms linear in C do not vanish. Thus, determining C by solving (33) for all (nearby) atom pairs (A, B) leads to errors for V linear in r (the same holds for DF in the RI-SVS approach). It has been concluded that the resulting errors are too large for the method to be useful in HF calculations.^{123,124,156} This might be true when standard auxiliary fit sets are used which are optimized for global DF. In principle, the error of the expansion (23) can always be made arbitrary small when an appropriate fit set is used although this is highly non trivial. Simply increasing the number of ABFs does not always result in reduced errors and might even lead to numerical instabilities in the fitting procedure due to an increase of linear dependencies in the auxiliary basis.¹⁶²

Another difficulty arises from the presence of diffuse functions in the AO-basis set. To understand the source of the problem, we recall that very large AO basis sets with many diffuse functions might be locally overcomplete which causes almost linear dependence of a subset of basis functions. These lead to numerical instabilities in the SCF¹⁹⁵ during canonical orthonormalization when the condition number of the AO-overlap matrix approaches infinity.¹⁹⁶ To restore numerical stability, one projects out the almost linearly dependent part from the basis by removing eigenvectors from the transformation matrix corresponding to eigenvalues of the AO-overlap matrix smaller than some threshold ϵ_D ,¹⁹⁷ effectively diminishing the basis set size. This is not a severe restriction in practice since numerical instabilities usually do not occur when all eigenvalues are larger than $\epsilon_D = 10^{-6} - 10^{-7}$.¹⁹⁸⁻²⁰⁰

Using PADF, numerical instabilities can already occur when all eigenvalues are considerably larger as has e.g. been observed for linear-response TDDFT with augmented basis sets²⁰¹ and MP2/QZ calculations.¹⁶² The reason for this behaviour is that individual fitting coefficients can become quite large for diffuse products from AOs centered on distant atoms. Note, that this is a fundamental difference to global DF. As a qualitative example, consider a linear alkane chain C_nH_{2n+2} and the pair product of a diffuse AOs on C_1 and C_n , respectively. The AOs will only have some (small) overlap in the middle of the chain. In global DF, this pair product could possibly be described very well with only a small set of

ABFs centered on atoms in this region. In PADF, this overlap needs to be described with the asymptotic tails of diffuse ABFs on C_1 and C_n . When there is no appropriate ABF in the auxiliary basis, this will lead to very large fitting coefficients for some (diffuse) ABFs. In the transformation of the Coulomb potential from auxiliary basis to AO-product basis, these large fitting coefficients must cancel with contributions with opposite sign which is numerically unstable.²⁰² Thus, relatively small errors might accumulate during the SCF and lead to an erroneous (hole) density matrix and potentially wrong eigenvalues.

To summarise, projecting out parts of the basis during canonical orthonormalization plays a dual role when PADF is used in the SCF. First, it ensures numerical stability of the SCF and second, as a side-effect, it removes the part of the basis which potentially results in diffuse AO-products which are potentially difficult to fit. This nicely illustrates that the appropriate choice of auxiliary basis and the problem of linear dependencies are intertwined. Adding more diffuse functions to the auxiliary basis the pair product in our example can be better approximated, the fitting coefficient become smaller, and the linear dependency problem is extenuated. This means, the number of AOs which needs to be removed becomes smaller and larger basis sets can be used in practice.

In the present work, we employ auxiliary fit sets which have been optimized for gKS calculations with PADF. Using these fit sets, we have shown recently^{162,163} that the accuracy of PADF-MP2 is similar to global DF-MP2 with GTOs for basis sets of up to TZ quality. On the other hand, using quadruple- ζ (QZ) and also smaller basis sets augmented with diffuse functions results sometimes in unreliable PADF-MP2 ground state energies. It is clear that the same issues will arise in GW calculations.

For correlated methods we observed, that a value of $\epsilon_D = 10^{-3}$, corresponding to a drastic truncation of the basis, seems to provide a good trade-off between accuracy and numerical stability for all basis sets beyond TZ quality and also augmented basis sets. However, while this truncation prevents collapse to artificially low QP energies, it also leads to deteriorated results compared to the default of $\epsilon = 10^{-4}$. Increasing the basis set more and more, larger

and larger parts of the virtual space need to be projected out which ultimately prevents us from reaching the complete basis set (CBS) limit for correlated methods. We expect, however, that carefully optimized auxiliary fit sets will enable the numerically stable application of PADF to these methods with larger basis sets. Before we discuss the accuracy of the present approach in section 3, we will describe in some detail how PADF can be used to implement eqs. (26)–(29) efficiently.

2.3 GW equations with pair atomic density fitting

In this section we outline how the sparsity of the map from \mathcal{P} to \mathcal{A} can be exploited to implement GW in a low-scaling fashion.

Imaginary time and frequency grids After calculation of the Coulomb potential and its inverse in the basis of ABFs and the basis transformation matrix C as described in section 2.2, we calculate imaginary frequency and imaginary time grids, $\{\omega_k\}_{k=1,\dots,N_\omega}$, $\{\tau_k\}_{k=1,\dots,N_\tau}$, respectively. As outlined by Kresse and coworkers,¹⁶⁴ they can be evaluated by minimizing either the L_∞ (Chebyshev) or L_2 norm of

$$\eta(\{\alpha, \beta\}, x) = \frac{1}{x} - f(\{\alpha, \beta\}, x), \quad f = \begin{cases} 2 \sum_{k=1}^{N_\tau} \alpha_k e^{-\beta_k x} & \beta = \tau \\ \frac{1}{\pi} \sum_{k=1}^{N_\omega} \alpha_k \frac{2x}{x^2 + \beta_k^2} & \beta = \omega \end{cases} \quad (37)$$

with respect to the parameter sets α, β , where $x \in [\epsilon_{min}, \epsilon_{max}]$, where ϵ_{min} (ϵ_{max}) denotes the smallest (largest) KS orbital energy difference. Imaginary time and imaginary frequency domain are connected through Laplace transforms (See also Cancs et al.¹⁷⁵),

$$f(i\tau) = \frac{i}{2\pi} \int d\omega f(i\omega) (\cos(\omega\tau) + i \sin(\omega\tau)) \quad (38)$$

$$f(i\omega) = -i \int d\tau f(i\tau) (\cos(\omega\tau) - i \sin(\omega\tau)). \quad (39)$$

For our purpose, it is sufficient to treat them as Fourier transforms. To avoid potentially inaccurate interpolation to equidistant grids in order to use discrete Fourier transforms, we discretize (39) as

$$f(i\omega_k) = -i \sum_j^{N_\tau} \left\{ \gamma_{kj}^{(c)} \cos(\omega_k \tau_j) (f(i\tau_j) + f(-i\tau_j)) - i \gamma_{kj}^{(s)} \sin(\omega_k \tau_j) (f(i\tau_j) - f(-i\tau_j)) \right\}, \quad (40)$$

where the weights $\gamma_{kj}^{(c)}$ and $\gamma_{kj}^{(s)}$ account for the non-uniformity of the grids. They are chosen to minimize the L_2 norm of the error introduced by (40) for $f(i\tau) = e^{-x|\tau|}$, $x \in [\epsilon_{min}, \epsilon_{max}]$, with respect to the exact transformation eq. (39). By inverting the matrices $\gamma_{kj}^{(c)} \cos(\omega_k \tau_j)$ and $\gamma_{kj}^{(s)} \sin(\omega_k \tau_j)$, respectively, one can use the same relation to transform f from imaginary frequency to imaginary time. To calculate the imaginary time grid, we minimize the L_∞ norm of (37) as implemented by Helmich-Paris et al.^{203,204} and in imaginary frequency we minimize the L_2 norm on a logarithmic grid using a Levenberg-Marquardt algorithm.^{205,206} Both algorithms require pretabulated values to converge to an acceptable local minimum. For the imaginary time domain, we use the values distributed with the source-code of Helmich-Paris et al.²⁰⁷ and for the imaginary frequency domain we tabulated our own values which we include in the supporting information.

Polarizability After the Green's function (15) and (16) have been constructed, P can be evaluated. In this section, we use $\mu, \nu, \kappa, \lambda$ to denote AOs, $\alpha, \beta, \gamma, \delta$ to denote ABFs, and the convention that $(\mu, \alpha) \in A$, $(\nu, \beta) \in B$, $(\kappa, \gamma) \in C$, $(\lambda, \delta) \in D$, where A, B, C, D label atoms. We denote the three-leg tensor collecting all fitting coefficients corresponding to all products formed from AOs centred on A and B and to ABFs centred on B as C^{ABB} , i.e. C^{ABB} contains only coefficients corresponding to fit-functions centred on B . Consequently, the fitting coefficient tensor corresponding to all products formed from AOs on A and B and to ABFs centred on A and B is split into $C^{ABB} + C^{BAA}$. We also define $C^{ABB} = \frac{1}{1+\delta_{AB}} \tilde{C}^{ABB}$ to avoid complications from double-counting. The contribution of each atom pair (A, B) to

P , eq. (26), is given as the sum of four contributions

$$P_{\alpha\beta,\tau}^{AB} = -i \left(P_{\alpha\beta,\tau}^{AB,I} + P_{\alpha\beta,\tau}^{AB,II} + P_{\alpha\beta,\tau}^{AB,III} + P_{\alpha\beta,\tau}^{AB,IV} \right) , \quad (41)$$

where

$$\begin{aligned} P_{\alpha\beta,\tau}^{AB,I} &= \sum_{\mu\nu\kappa\lambda} C_{\lambda\mu\alpha}^{DAA} \underline{G}_{\mu\kappa,\tau}^{DC} \overline{G}_{\nu\lambda,\tau}^{AB} C_{\nu\lambda\beta}^{CBB} \\ P_{\alpha\beta,\tau}^{AB,II} &= \sum_{\mu\nu\kappa\lambda} C_{\lambda\mu\alpha}^{DAA} \underline{G}_{\mu\kappa,\tau}^{AC} \overline{G}_{\nu\lambda,\tau}^{DB} C_{\nu\lambda\beta}^{CBB} \\ P_{\alpha\beta,\tau}^{AB,IV} &= \sum_{\mu\nu\kappa\lambda} C_{\lambda\mu\alpha}^{DAA} \underline{G}_{\mu\kappa,\tau}^{AB} \overline{G}_{\nu\lambda,\tau}^{DC} C_{\nu\lambda\beta}^{CBB} . \end{aligned} \quad (42)$$

As \underline{G} and \overline{G} are symmetric, the symmetry of the Kronecker product implies that P is symmetric as well and consequently $P^{AB,III} = [P^{BA,II}]^T$ and $P^{AB} = [P^{BA}]^T$. Also note, that $\text{Re}(P) = 0$. Defining the intermediates

$$\underline{F}_{\mu\nu\beta,\tau}^{ABB} = \sum_{\kappa} \underline{G}_{\mu\kappa,\tau}^{AC} C_{\kappa\nu\beta}^{CBB} \quad (43)$$

$$\overline{F}_{\mu\nu\beta,\tau}^{ABB} = \sum_{\kappa} \overline{G}_{\mu\kappa,\tau}^{AC} C_{\nu\kappa\beta}^{CBB} \quad (44)$$

$$\underline{H}_{\mu\kappa\beta,\tau}^{ACB} = \sum_{\nu} \underline{F}_{\mu\nu\beta,\tau}^{ABB} \overline{G}_{\nu\kappa,\tau}^{BC} \quad (45)$$

$$\overline{H}_{\mu\kappa\beta,\tau}^{ACB} = \sum_{\nu} \overline{F}_{\mu\nu\beta,\tau}^{ABB} \underline{G}_{\nu\kappa,\tau}^{BC} , \quad (46)$$

(42) is most conveniently evaluated as

$$\begin{aligned} P_{\alpha\beta,\tau}^{AB,I} + P_{\alpha\beta,\tau}^{AB,IV} &= \sum_{\nu\kappa} \left(\underline{H}_{\kappa\nu\alpha,\tau}^{CBA} + \overline{H}_{\kappa\nu\alpha,\tau}^{CBA} \right) C_{\kappa\nu\beta}^{CBB} \\ P_{\alpha\beta,\tau}^{AB,II} &= \sum_{\mu\nu} \overline{F}_{\nu\mu\alpha,\tau}^{BAA} \underline{F}_{\mu\nu\beta,\tau}^{ABB} . \end{aligned} \quad (47)$$

We parallelize the outermost loop over all atoms and perform all tensor contractions using level-3 BLAS. No step involves more than three atomic centers and since tensor contractions corresponding to distant centers (for which all elements in C are zero) can be skipped, the

operation count scales asymptotically as N^2 . We always evaluate the intermediates eqs. (43)–(46) on the fly since storage of 2-center quantities with more than 2 indices would quickly become prohibitive.

Screened Coulomb interaction After having evaluated P for all atom pairs, \widetilde{W} can be evaluated as in conventional approaches using matrices of dimension $N_{aux} \times N_{aux}$. After transforming the matrix P (which is even in imaginary time) to the imaginary frequency axis using (40), the screened interaction \widetilde{W}_ω is obtained by inversion,

$$\widetilde{W}_\omega = [V^{-1} - P_\omega]^{-1} - V. \quad (48)$$

For all ω , W is stored in distributed memory. Note, that on the imaginary frequency axis, $\text{Im}(P) = 0$ and thus $\text{Im}(\widetilde{W}) = 0$ as well. To evaluate (48), the dielectric function is not constructed explicitly as it would not be symmetric and its inversion would be computationally demanding. We invert $V^{-1} - P_\omega$ (and V which only needs to be done once) using an LU decomposition with partial pivoting as implemented in SCALAPACK. Note, that inversion using CD would be numerically unstable since C might not be full-rank and thus does not necessarily conserve positive semi-definiteness. We subsequently transform \widetilde{W} back to imaginary time.

Self-energy Next, the contributions to Σ for all atom pairs,

$$\Sigma_{\mu\nu,\tau}^{c,AB} = i (\Sigma_{\mu\nu,\tau}^{AB,I} + \Sigma_{\mu\nu,\tau}^{c,AB,II} + \Sigma_{\mu\nu,\tau}^{c,AB,III} + \Sigma_{\mu\nu,\tau}^{c,AB,IV}), \quad (49)$$

are evaluated, where $\Sigma^{AB,III} = [\Sigma^{BA,II}]^T$, $\Sigma^{AB} = [\Sigma^{BA}]^T$. Also, $\text{Re}(\Sigma^c) = 0$, since $\text{Re}(G) = 0$ and $\text{Re}(\widetilde{W}) = 0$. We only give here the equations for $\Sigma^c(i\tau)$ as Σ^x is obtained in exactly the same way by replacing \widetilde{W} with V and using $\underline{G}(i\tau = 0)$. As Σ is an uneven function in imaginary time, we also need to evaluate $\Sigma(-i\tau)$ to be able to Fourier transform it to

the imaginary frequency axis. The corresponding equations can be retrieved from the ones for $\Sigma(i\tau)$ by simply exchanging \underline{G} with \bar{G} and replacing upper bars with lower bars in all intermediates. To express the individual contributions to Σ we define the intermediate

$$I_{\mu\nu\gamma,\tau}^{ABC} = C_{\mu\nu\beta}^{ABB} \widetilde{W}_{\beta\gamma,\tau}^{BC}, \quad (50)$$

and together with (44) and (43) we obtain

$$\underline{\Sigma}_{\mu\kappa,\tau}^{c,AC,I} = \sum_{\nu\lambda} \sum_{\alpha\gamma} \underline{G}_{\lambda\nu,\tau}^{DB} C_{\lambda\mu\alpha}^{DAA} \widetilde{W}_{\alpha\gamma,\tau}^{AC} C_{\nu\kappa\gamma}^{BCC} = \sum_{\nu\alpha} \underline{F}_{\nu\mu\alpha,\tau}^{BAA} I_{\nu\kappa\alpha,\tau}^{BCA} \quad (51)$$

$$\underline{\Sigma}_{\mu\kappa,\tau}^{c,AC,II} = \sum_{\nu\lambda} \sum_{\alpha\beta} \underline{G}_{\lambda\nu,\tau}^{DB} C_{\lambda\mu\alpha}^{DAA} \widetilde{W}_{\alpha\beta,\tau}^{AB} C_{\kappa\nu\beta}^{CBB} = \sum_{\nu\alpha} \underline{F}_{\nu\mu\alpha,\tau}^{BAA} I_{\kappa\nu\alpha,\tau}^{CBA} \quad (52)$$

$$\underline{\Sigma}_{\mu\kappa,\tau}^{c,AC,IV} = \sum_{\nu\lambda} \sum_{\delta\beta} \underline{G}_{\lambda\nu,\tau}^{DB} C_{\mu\lambda\delta}^{ADD} \widetilde{W}_{\delta\beta,\tau}^{DB} C_{\kappa\nu\beta}^{CBB} = \sum_{\lambda\delta} \left[\sum_{\nu} \underline{G}_{\lambda\nu,\tau}^{DB} I_{\kappa\nu\delta,\tau}^{CBD} \right] C_{\mu\lambda\delta}^{ADD}. \quad (53)$$

As for P we parallelize the outermost loop over all atoms and completely rely on level-3 BLAS for all tensor contractions. Due to its prefactor of $N_{AO,l}^2 \times N_{aux,l}^2$, where $N_{aux,l}$ ($N_{AO,l}$) denote the number of ABFs (AOs) on on atomic center, the calculation of I is the most expensive step. The asymptotic operation count can be reduced significantly as the screened interaction \widetilde{W} , unlike the Coulomb interaction, decays exponentially as direct consequence of the exponential decay of the Green's function. In our current implementation, we do not fully exploit this property as we essentially treat \widetilde{W} like the bare Coulomb potential in the calculation of Σ^x . In the same way as for C , we can skip all tensor contractions for approximately non-Coulomb-interacting atom pairs. For weakly interacting pairs, we rely on multipole expansions of the Coulomb potential to reduce the prefactor of all contractions involving W (and V for Σ^x) considerably so that Σ can also be evaluated with quadratic operation count. Fully exploiting the exponential decay of \widetilde{W} , the asymptotic scaling can possibly be reduced further.

Quasi-particle equations Σ^c is subsequently transformed to the MO basis and its diagonal elements to imaginary frequency space. With (40),

$$\Sigma_{nn,\omega_k}^c = -i \sum_j \gamma_{kj}^{(c)} \cos(\omega_k \tau_j) \left[\underline{\Sigma}_{nn,\tau_j}^c + \bar{\Sigma}_{nn,\tau_j}^c \right] - \sum_j \gamma_{kj}^{(s)} \sin(\omega_k \tau_j) \left[\underline{\Sigma}_{nn,\tau_j}^c - \bar{\Sigma}_{nn,\tau_j}^c \right], \quad (54)$$

from which the QP equation (10) is solved. We analytically continue (AC) Σ_{nn}^c to the real frequency axis using a Padé-approximant of order N_ω as described by Vidberg and Serene²⁰⁸ and solve (10) for all states of interest using bisection. While the present approach is not applicable to core level excitations,^{45–47} it predicts QP energies in the valence region with good accuracy in case the QP solution is sufficiently distant from any pole of the self-energy.^{46,133,209,210} This is always the case for molecules with a large KS HOMO-LUMO gap. Note, that in these cases small imaginary frequency grids are sufficient to ensure good accuracy for particle and hole states in the valence region.

To summarize this section, a pseudocode of our implementation together with theoretical asymptotic scaling with system size is given in figure 1.

Algorithm 1 Pseudocode for G_0W_0 using PADF. The asymptotic operation count of some key steps is given on the right.

Input MO coefficients $b_{\mu n}$, orbital energies, ϵ_n from (1)	
Compute C, V, V^{-1}	
Compute $\{\tau_i\}_{i=1,\dots,N_\tau}, \{\omega_k\}_{k=1,\dots,N_\omega}, \left\{ \gamma_{ki}^{(c)}, \gamma_{ki}^{(s)} \right\}_{k=1,\dots,N_\omega, i=1,\dots,N_\tau}$	
for $\tau = \tau_1, \tau_2, \tau_3 \dots, \tau_{N_\tau}$ do	
Calculate G using (15), (16)	$N^3 N_\tau$
for $A \in N_{atom}, B \in N_{atom}$ do	
Evaluate $P^{AB}(\tau_i)$ using (41)-(47)	$N^2 N_\tau$
end for	
for $\omega = \omega_1, \omega_2, \omega_3 \dots, \omega_{N_\omega}$ do	
Calculate contribution to $P(\omega_i)$ using (40)	$N^2 N_\tau N_\omega$
end for	
end for	
for $\omega = \omega_1, \omega_2, \omega_3 \dots, \omega_{N_\omega}$ do	
Calculate $W(\omega_k)$ using (48)	$N^3 N_\omega$
end for	
for $\tau = \tau_1, \tau_2, \tau_3 \dots, \tau_{N_\tau}$ do	
for $\omega = \omega_1, \omega_2, \omega_3 \dots, \omega_{N_\omega}$ do	
Calculate $W(\tau_i)$ using (40)	$N^2 N_\tau N_\omega$
end for	
for $A \in N_{atom}, B \in N_{atom}$ do	
Evaluate $\Sigma^{AB}(\tau_i)$ using (49) to (53)	$N^2 N_\tau$
end for	
Calculate Σ_{nn,τ_i} and evaluate (54)	
end for	
Evaluate QP-spectrum using (10)	

3 Results

3.1 Computational Details

All calculations have been performed with a locally modified development version of ADF^{172,173} in which the herein described PADF- G_0W_0 algorithm has been implemented. In all gKS calculations, PADF has been used to evaluate Coulomb- and exchange terms.^{149,150,211} We performed PADF- G_0W_0 @PBE and PADF- G_0W_0 @PBE0 calculations for all molecules in the GW100 database⁸² as well as PADF- G_0W_0 @PBE0^{212,213} calculations for the 50 largest molecules in the GW5000 database.²¹⁴ For GW100, we used the structures as published

in the original work,⁸² except for Vinylbromide and Phenol for which we used the updated structures.²¹⁵ To preclude potential confusion, we emphasize that all results from other codes we refer to herein have been taken from the literature and have not been calculated by us.

We herein use several all-electron (AE) STO-type basis sets of double- ζ (DZ), TZ, and QZ size. The prefix “aug-” denotes augmentation of a basis set with an additional shell of diffuse functions for all angular momenta $l = 0, 1, 2$. For augmented QZ basis sets, an additional diffuse shell of f-functions is added as well. Augmentation of the basis set with x additional shells of polarization functions is denoted by xP . We employ two different QZ basis sets, the even-tempered QZ3P²¹⁶ basis set, and the larger QZ4P²¹⁷ basis set. For a detailed description of the basis sets we refer to van Lenthe et al.²¹⁷ It should be noted, however, that all basis sets are not correlation consistent (CC) and unsuitable for CBS limit extrapolation. Also note, that QZ3P and all augmented basis sets are only available for the first 4 rows of the periodic table. In case of QZ3P we will use QZ4P for all heavier elements and in case of augmented basis sets we use the respective basis set without augmentation.

If not indicated otherwise, we used the *Normal* auxiliary fit set,²¹⁸ *Good* quality for numerical integration,²¹¹ *Normal* quality for thresholds controlling distance effects, and standard numerical settings otherwise. We use imaginary time and frequency grids with up to $N_\omega = 18$ points each²¹⁹ for GW100 and $N_\omega = 16$ points each for GW5000 and use a pad-approximant of order N_ω to model the self-energy on the real frequency axis. In all $G_0W_0@PBE0$ calculations on GW5000 we employed the unscaled Zero Order Regular Approximation (ZORA).^{220–223}

During orthonormalization of the Fock matrix in the SCF, columns of the transformation matrix are removed when the corresponding eigenvalues of the AO-overlap matrix are smaller than some threshold ϵ_D .¹⁹⁶ As explained above, we have adjusted this value to $\epsilon_D = 10^{-3}$ in all calculations using QZ4P or augmented basis sets. Otherwise, the default of $\epsilon_D = 10^{-4}$ has been used.

3.2 Benchmarks

3.2.1 The GW100 database

The size and type of basis set is the most crucial factor influencing the results of a GW calculation.⁸² Using localized basis functions, even on the QZ level BSEs for HOMO and especially LUMO QP energies can exceed several hundreds meV, necessitating an CBS limit extrapolation to obtain very accurate reference values.^{46,82,214} Using localized AOs one needs to rely on heuristics since the expansion of MOs in this basis does not converge uniformly, unlike expansions in terms of PW²²⁴ or finite elements in RS.²²⁵ HOMO QP energies obtained with these basis set types are generally in good agreement with the original ones by van Setten et al.,⁸² while differences for unbound LUMO energies often exceed 1 eV.^{210,226,227}

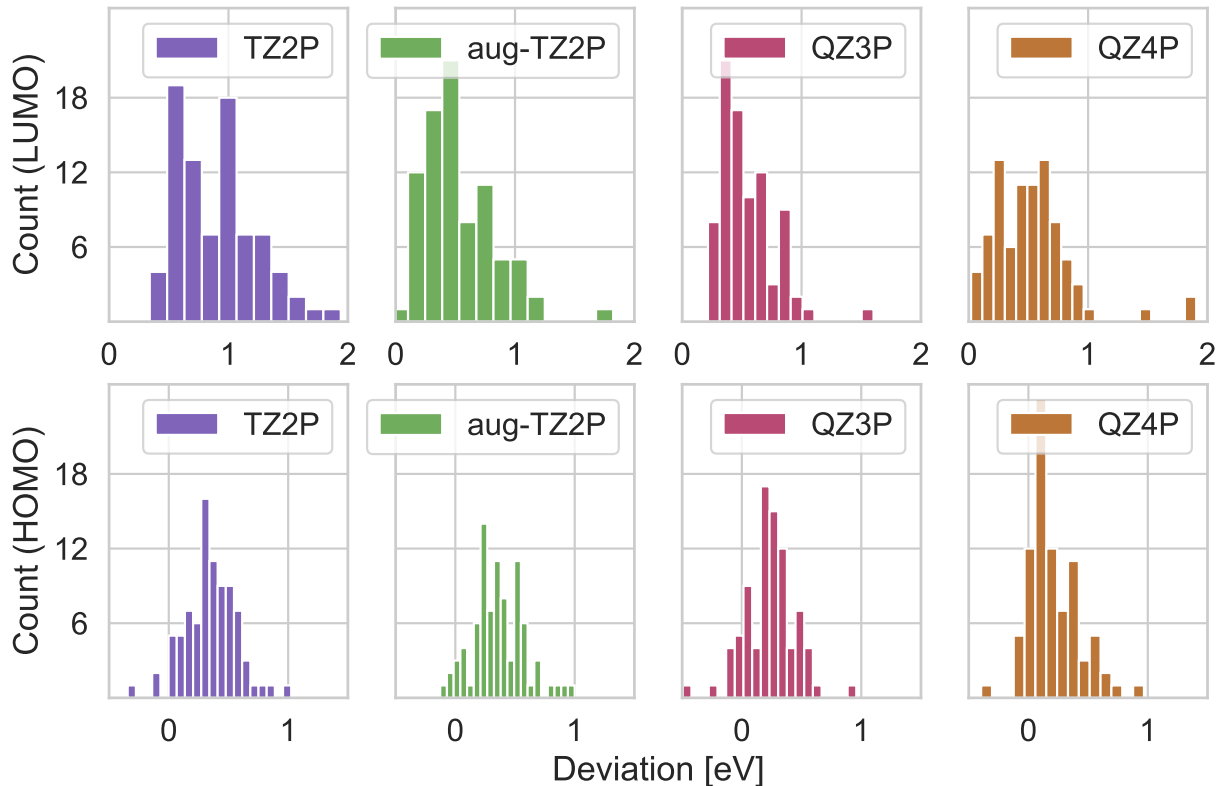


Figure 1: Error distributions (in eV) for G_0W_0 @PBE with four different STO-type basis sets for the HOMO (bottom) and LUMO QP energies (top) in the GW100 database with respect to the nanoGW reference. Due to its error larger than 3 eV, CO_2 is not included in the upper left plot.

Thus, it is not straightforward for our purpose to chose appropriate reference values and we will therefore use more than one reference in the following. As primary reference for GW100 we use RS results²²⁸ by Chelikowsky and coworkers.²²⁷ While these results are not extrapolated to the CBS limit, they are carefully converged and should be a very reliable reference. This choice is mainly motivated by the large differences between plane-wave and GTO implementations for unbound LUMO energies. It has been argued by Kresse and coworkers²²⁶ that the GTO-type basis sets of the def2 family might not be flexible enough to adequately describe these QP energies and lead to significantly overestimated unbound LUMO energies. On the other hand, the nanoGW results deviate to WEST/VASP by only 134/122 meV for GW100, only excluding all noble gases and H₂ but including all other molecules with unbound LUMOs.²²⁷ While in comparisons between different codes these systems are often excluded,²¹⁰ we decided to retain them in this work as well. However, we excluded from our analysis all noble gases and H₂ since for these molecules the discrepancies between RS, PW-pseudopotential and AE codes often exceed 2 eV.^{82,210,226,227} We also excluded Cl₄, KBr, NaCl, BN, O₃, BeO, MgO, Cu₂ and CuCN for which multiple solutions can be found when the QP equation (10) is solved for the HOMO. This leaves us with a set of 85 molecules which we will discuss in the following. In section 3.2.2, we benchmark our implementation against reference results obtained with GTOs for a large number of organic molecules with bound LUMOs.

The histograms in figure 1 summarize the results of our benchmarks on GW100 and shows errors obtain with our implementation and different basis sets with respect to the nanoGW reference. For individual QP energies we refer to the supporting information. Figure 2 shows MADs for the HOMO QP energies between different codes and basis sets. Since we are not able to perform basis set extrapolation, the QZ4P results are the best ones attainable for us. We observe MADs of 0.24 eV with respect to the nanoGW²²⁹ results and of 0.32 eV to the CBS limit extrapolated (CBSLE) FHI-AIMS^{68,69,134} QP energies. With respect to both, the RS and the FHI-AIMS CBS limit, QZ4P yields an accuracy comparable to TURBOMOLE²³⁰

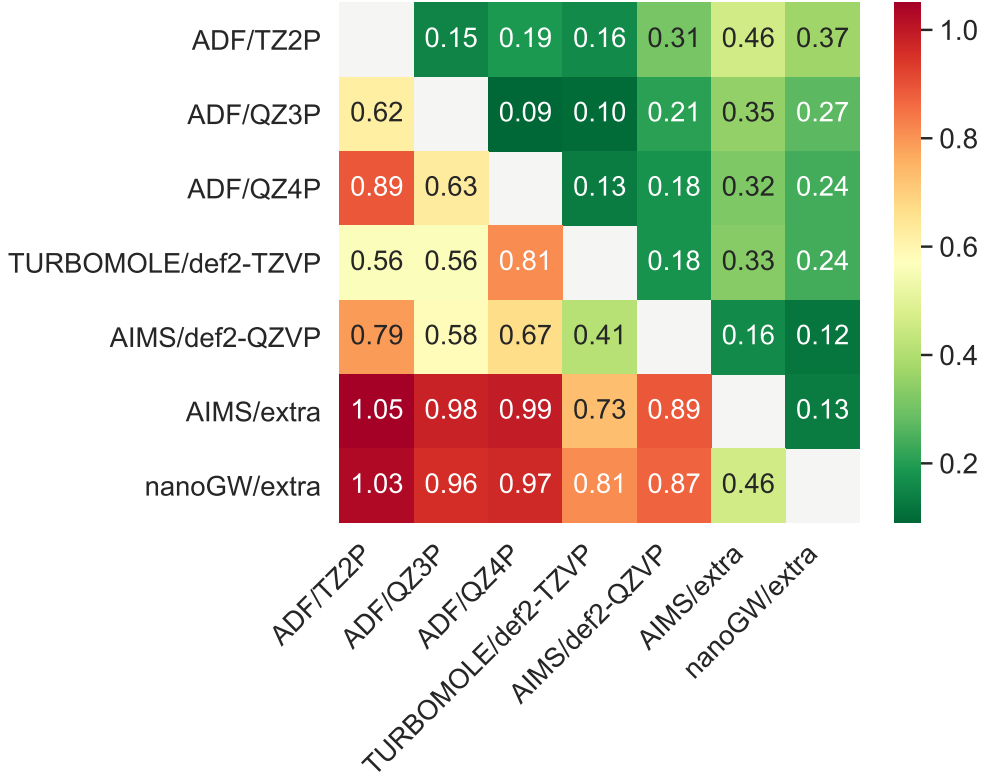


Figure 2: MADs (upper triangle) and maximum absolute deviations (lower triangle) in eV of QP HOMO energies computed with different codes and basis sets, specified on the axes for G_0W_0 @PBE.²¹⁵

with the smaller def2-TZVP basis set (6th and 7th column in the heatmap in figure 2). QZ4P does not give significant improvements over QZ3P and with a MAD of 0.12 eV with respect to the nanoGW reference, def2-QZVP performs considerably better than QZ4P. The fact that the former one has more polarization functions (e.g. (7s,4p,3d,2f,1g) vs. (7s,4p,2d,2f) for second row elements²³¹) might explain part of the discrepancy. Furthermore, the excessive truncation of the QZ4P-basis in the canonical orthonormalization procedure during the SCF effectively diminishes the size of the virtual space. This might also explain why QZ4P only improves moderately over the significantly smaller TZ2P basis set (0.46 vs. 0.32 eV) while going from def2-TZVP to def2-QZVP reduces the MAD with respect to both CBS limits by roughly 50 %. Also a visual inspection of the error distributions for the QZ3P and QZ4P QP HOMO energies in figure 1 reveals that the QZ4P-errors shows a larger spread and more

often exceed 0.5 eV than for QZ3P.

Table 1: MADs of the G_0W_0 @PBE HOMO and LUMO QP energies corresponding to figure 1 and HOMO-LUMO gaps with respect to the CBS limit for four different STO-type basis sets (All values in eV).

	TZ2P	aug-TZ2P	QZ3P	QZ4P
HOMO	0.37	0.37	0.27	0.24
LUMO	0.94	0.55	0.56	0.52
gap	0.59	0.26	0.34	0.35

For the LUMO QP energies shown in the upper part of figure 1, aug-TZ2P, QZ3P and QZ4P show comparable MADs of 0.55, 0.56 and 0.52 eV, respectively and thus improve significantly over TZ2P with a MAD of nearly 1 eV (see table 1). For TZ2P and both QZ basis sets, the MAD of the LUMO QP energies with respect to the RS reference values are more than twice as large than for the HOMO which results in a rather poor description of the HOMO-LUMO gap. This behaviour is similar to the performance of the def2 family of GTO-type basis sets for GW100 for which the errors for the LUMO are on average roughly twice as large than for the HOMO.⁸² aug-TZ2P overestimates HOMO and LUMO QP energies most symmetrically and consequently, with a MAD of 0.26 eV, describes the HOMO-LUMO gap significantly better than both QZ basis. The situation is well known from augmented GTO-type basis sets^{73,209,232–235} which usually converge considerably faster to the CBS HOMO-LUMO gap than non-augmented basis sets,²⁰⁹ although the individual HOMO and LUMO levels are often not converged at all.

Finally, we investigate some LUMO QP energies with exceptionally slow convergence to the CBS limit in more detail and see whether convergence can be attained using larger basis sets, keeping in mind the restrictions imposed by the PADF as explained in section 2; reaching the basis set limit is only possibly for us for very small systems. While the CO_2 LUMO QP energy deviates from the CBS limit by more than 3 eV, also for F_2 , CF_4 C_3H_3 and $\text{C}_n\text{H}_{2n+2}$ for $n = 1, \dots, 4$, the TZ2P LUMO QP energies deviate between 1.7 eV and 1.4 eV from the CBS limit. We investigate the convergence with respect to the basis set size for

these molecules (except for Propane and Butane) in figure 3 by adding diffuse functions to the QZ3P basis set.

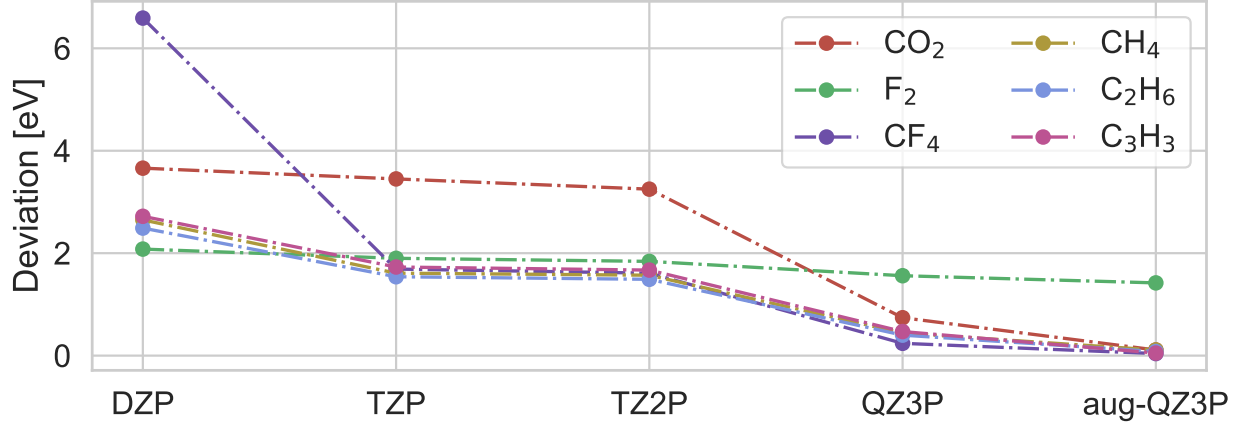


Figure 3: Deviations of G_0W_0 @PBE LUMO QP energies to the CBS limit for six selected molecules from the GW100 database for different STO-type basis sets (all values in eV).

For all molecules except F_2 , our aug-QZ3P results agree very well with the RS reference values. This is a little surprising since the GTO-type basis set CBSLE results differ by more than 1 eV for CH_4 , C_2H_6 and C_3H_3 . In fact, not only for these systems we observe that our unbound LUMO energies are generally closer to RS and PW than to GTO references. While being out of the scope of this work, this is an interesting observation which deserves further investigation. For F_2 , the extrapolated CBS limits from different codes are in good agreement and the errors from aug-QZ3P are still hard to explain with BSEs alone, although van Setten et al. found a BSE of 0.53 eV for the LUMO energy using def2-QZVP.⁸²

3.2.2 The GW5000 database

We now turn our attention to systems large enough for local approximations to take effect and discuss the HOMO and LUMO energies of 20 organic molecules with between 85 and 99 atoms from the GW5000 database.²¹⁴ These tests are crucial for our purpose. First, they allow us to assess the effect of the values of the thresholds controlling distance effects. As explained in detail elsewhere,¹⁶² we essentially rely on three thresholds in our implementa-

tion, which we organize in three tiers, denoted as *Basic*, *Normal* and *Good*. For the exact values of these thresholds we refer to the supporting information.

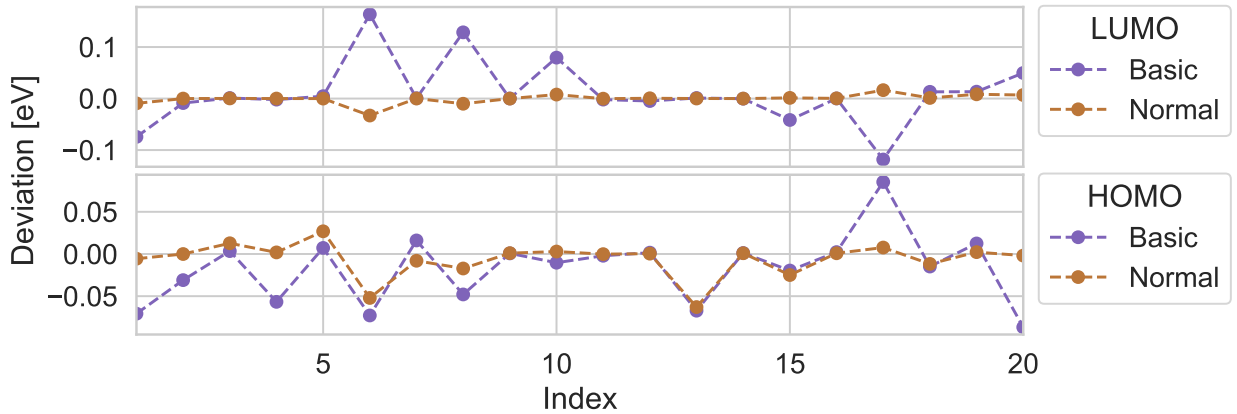


Figure 4: Deviations of the *Basic* and *Normal* threshold tiers with respect to the *Good* tier for HOMO (bottom) and LUMO (top) QP energies on the G_0W_0 /PBE0 level of theory (all values in eV).

The convergence with respect to the threshold tiers for HOMO and LUMO QP energies is shown in figure 4. As shown in the lower panel, the HOMO energies from different threshold tiers agree within 0.1 eV and the HOMO energies from the *Normal* and the *Good* threshold tier usually agree within an accuracy of 60 mEV. Using the *Basic* threshold tier, the LUMO QP energies show a maximum deviation of roughly 0.15 meV with respect to the *Good* tier. On the other hand, the LUMO energies from the *Normal* and *Good* tier are in even better agreement than the corresponding HOMO energies. Thus, using the *Normal* tier ensures an internal precision of our implementation of 60 meV for HOMO and LUMO QP energies. In case only the HOMO level is of interest, sufficient precision is already attained using the *Basic* threshold tier.

Second, the applicability of our implementation to the small molecules in GW100 does not imply the same for larger systems. In fact, this is true for any method exploiting locality in any form. Due to the reasons outlined in section 2 we refrain from reporting results with QZ and large augmented basis sets for these systems. Instead, we want to investigate the accuracy attainable using the TZ2P and aug-DZP basis sets for which no numerical problems

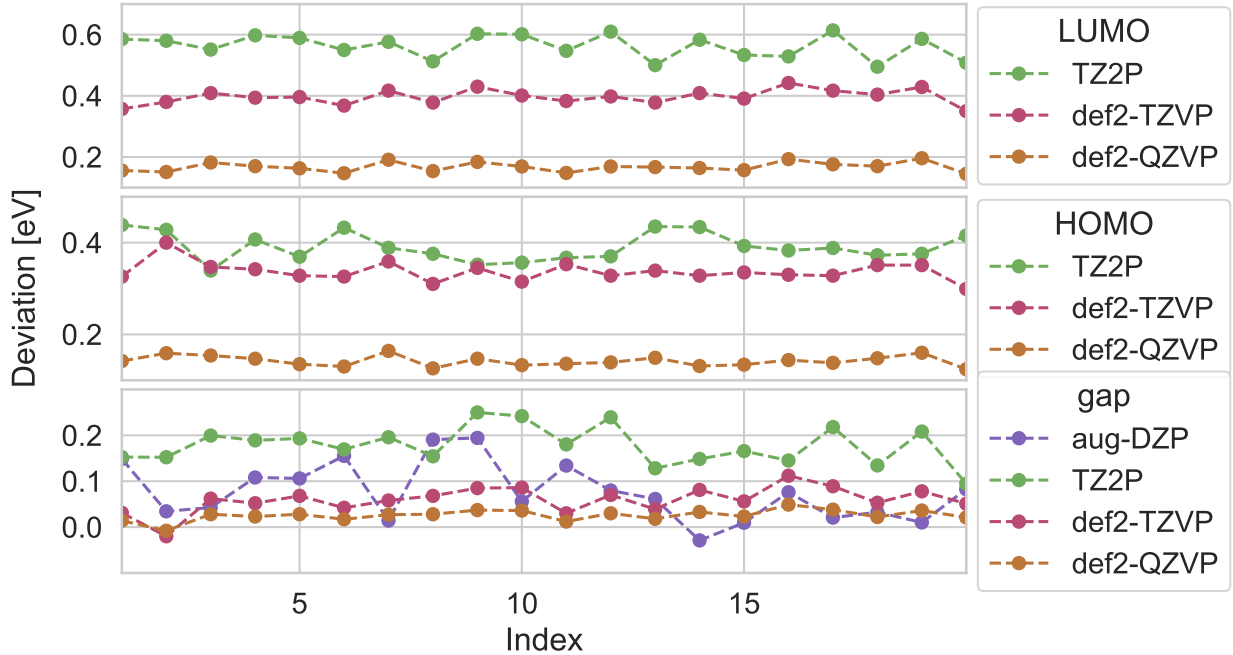


Figure 5: Deviations of LUMO (upper panel) QP energies, HOMO (middle panel) QP energies and HOMO-LUMO QP gaps (lower panel) for the TZ2P (*Normal* thresholds) as well as the GTO-type def2-TZVP and def2-QZVP basis sets with respect to the CBS limit for the HOMO energies of the 20 large molecules from the GW5000 database. HOMO-LUMO QP gaps from aug-DZP are shown as well. All values are in eV).

can be expected also for large molecules.

Table 2: MADs of HOMO energies, LUMO energies and HOMO-LUMO gaps with respect to the CBS limit for the 20 considered molecules from the GW5000 database for different basis sets. The *Normal* tier of thresholds has been used in all PADF- G_0W_0 calculations. All values are in eV.

	TZVP	QZVP	TZ2P	aug-DZP
HOMO	0.34	0.14	0.39	0.46
LUMO	0.40	0.17	0.56	0.53
gap	0.06	0.03	0.18	0.08

We compare our results for QP HOMO and LUMO levels as well as HOMO-LUMO gap for the 20 selected molecules to accurate reference values calculated with numerical GTOs with the FHI-AIMS code in figure 5. MADs for these quantities with respect to the CBS limit are given in table 2. We observe that the TZ2P HOMO QP energy never deviates from

def2-TZVP by more than 0.1 eV and the MAD of 0.39 eV is only 50 meV higher than the one found for def2-TZVP. For the LUMO energy, the situation is different. While def2-TZVP yields a MAD of 0.40 eV for this quantity, TZ2P performs with 0.56 eV considerably worse. This has a profound effect on the description of the HOMO-LUMO gap. Since def2-TZVP overestimates the LUMO level not much more than the HOMO QP energy, the HOMO-LUMO gap shows with a MAD of 0.06 eV an excellent agreement to the CBS limit while TZ2P yields a MAD of 0.17 eV. On the other hand, using the smaller aug-DZP basis set we find with a MAD of 0.08 eV good agreement with the CBS limit. As might be inferred from table 2, this success results mainly in poorer description of the HOMO level compared to TZ2P and the error cancellation between HOMO and LUMO is not always reliable, which can be seen from systems #8 and #9 whose HOMO-LUMO gap differs to the CBS limit by 0.2 eV. It should also be noted, that def-DZP calculations are slightly slower than TZ2P ones for medium and large systems since more AO-pair products need to be considered.

Finally, we investigate the accuracy of our algorithm as a function of systems size. To this end, we randomly selected 250 molecules from the GW5000 database and sorted these systems from smallest (12 atoms) to largest (99 atoms). Figure 6 shows the deviations to the CBS limit of our G_0W_0 @PBE0 results for HOMO, LUMO and HOMO-LUMO QP gap with the TZ2P and aug-DZP basis sets as well as FHI-AIMS results using the def2-TZVP and def2-QZVP basis sets.²¹⁴ Additionally, we performed linear fits as implemented in Numpy, which are also shown in figure 6. Essentially we obtain the same picture as for the 20 large molecules: TZ2P performs nearly as good as def2-TZVP for the HOMO QP energies and considerably worse for the LUMO level which translates into a worse description of the HOMO-LUMO gap. While it is observed that the STO-results show a larger spread than their GTO counterparts especially for LUMO energies, we also observe that the deviation to the CBS limit decreases with growing system size for all basis sets. For all subplots in figure 6, the TZ2P fit is more or less parallel (also see the fit-parameters in the supporting information for comparison) to the GTO-fits, while the slope in the aug-DZP fit for the

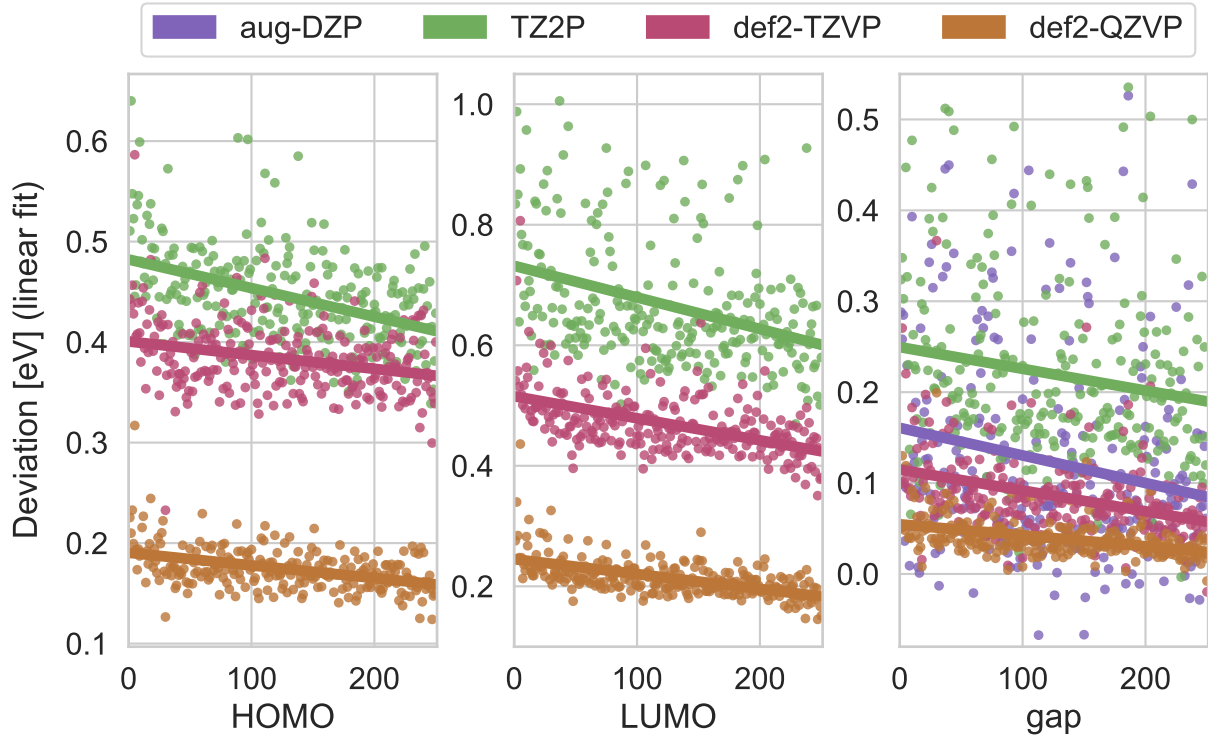


Figure 6: HOMO (left), and LUMO QP energies (middle) as well as HOMO-LUMO QP gaps (right) with different basis sets for 250 randomly selected molecules from the GW5000 database (dots) as well as linear fits, $f(x) = a \times x + b$. The systems have been sorted according to increasing size.

HOMO-LUMO gap is slightly more negative. As for the subset of 20 large molecules, aug-DZP produces HOMO-LUMO gaps which on average agree with the CBSLE reference within 0.15 eV for systems larger than a few tens of atoms. However, in some cases the errors can still be rather large (e.g. larger than 0.4 eV in 7 out of 250 cases), while the def2-QZVP BSE practically never exceeds 0.1 eV.

The decreasing errors are most likely due to basis set superposition which leads to a more complete basis when the system increases and the assumption that this effect is more pronounced for basis sets with many diffuse functions such as aug-DZP is reasonable. Thus, we can conclude that the accuracy of our algorithm is not negatively affected by the system size. We note, that local over-completeness and the associated numerical issues can already be encountered for very small systems like the ones the left side of the plots in figure 6. On

the other hand, it is highly unlikely that they become more pronounced for larger systems due to the locality of the AOs.

3.3 Representative timings

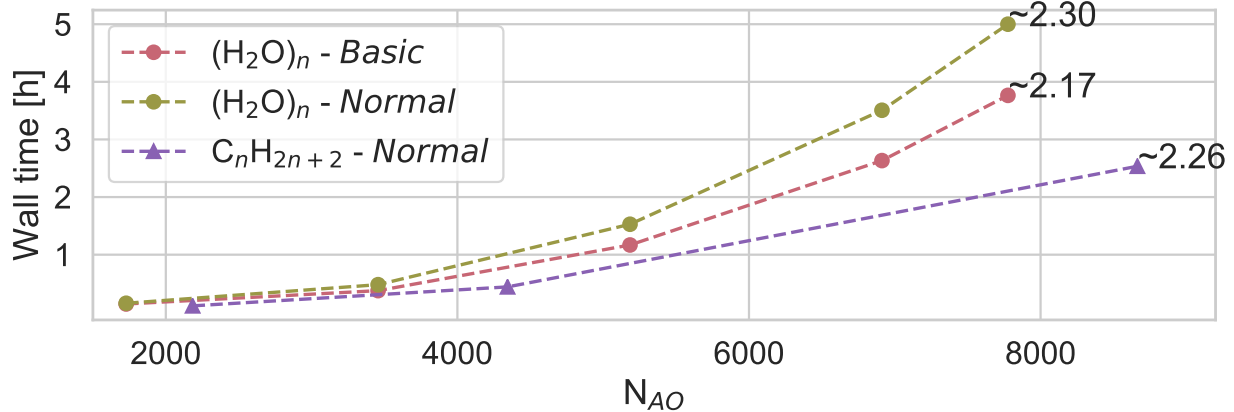


Figure 7: Wall times in hours for G_0W_0 @PBE/TZ2P calculations on a series of Water clusters and a linear alkane chain (exclusive the preceding SCF). All calculations have been performed on 2 bw nodes. The exponent of the polynomial describing the asymptotic scaling of the algorithm is given on the right of each plot.

In order to analyse the asymptotic scaling of our algorithm, we present G_0W_0 @PBE/TZ2P calculations on series of water clusters²³⁶ using the same numerical settings as for GW5000, the *Basic* and *Normal* tiers of thresholds and 12 imaginary time and imaginary frequency points. All calculations presented in this subsection were performed on 2.2 GHz intel Xeon (E5-2650 v4) nodes (broadwell architecture) with 24 cores and 128 GB RAM each (bw nodes in short). Figure 7 shows the wall times for the G_0W_0 -part of the calculations and the exponents of the polynomials describing the asymptotic scaling of these calculations with increasing system size. Information on CPU time and asymptotic scaling of key steps of the algorithm for the largest of these systems are given in figure 8

The largest water cluster here comprises 432 atoms with 7776 AOs and 36576 ABFs. Using the *Normal* threshold tier, the whole G_0W_0 calculation takes five hours on two nodes. As shown in figure 8, the most expensive step is the calculation of Σ , being responsible

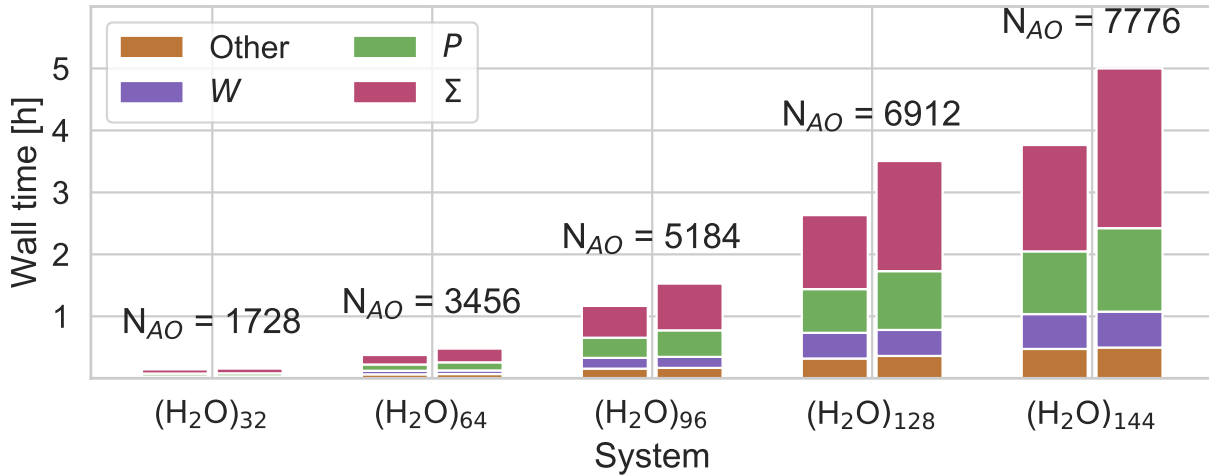


Figure 8: Contributions to total G_0W_0 wall times from different key steps for a series of Water cluster using the TZ2P basis set. Left bar in each group: *Basic* threshold quality, right bar in each group: *Normal* threshold quality. All calculations have been performed on 2 bw nodes.

for about half of the wall time of the whole calculation, followed by the evaluation of P . The evaluation of Σ is also the step which is accelerated most when the thresholds are loosened. This is due to the contractions eq. (50) which are tremendously accelerated when the multipole approximation is used for an increasing number of atom pairs. Consequently, the asymptotic scaling of this step is decreased from $N^{2.34}$ to $N^{2.15}$. Also the asymptotic scaling of P is reduced considerably (from $N^{2.19}$ to $N^{2.05}$), so that the wall time of the total calculation can be reduced to less than 4 hours. The evaluation of W is not affected by changing the thresholds, however, due to its low prefactor it can not be expected to become a bottleneck even for systems larger than the ones considered here.

Water clusters are very compact systems due to their spherical shapes. This takes an adverse effect on the asymptotic scaling properties of our algorithm, compared to low-dimensional systems, e.g. linear alkane chains as the most extreme example. The timings for a series of alkane chains is given for comparison in figure 7 as well. With the same thresholds, the G_0W_0 -calculation for $C_{160}H_{322}$ takes with roughly 2.5 hours only half the time as the one for $(H_2O)_{144}$ even though the former system is larger. In fact, P is calculated in less than

half an hour which is less wall time than is required for the calculation of \widetilde{W} .

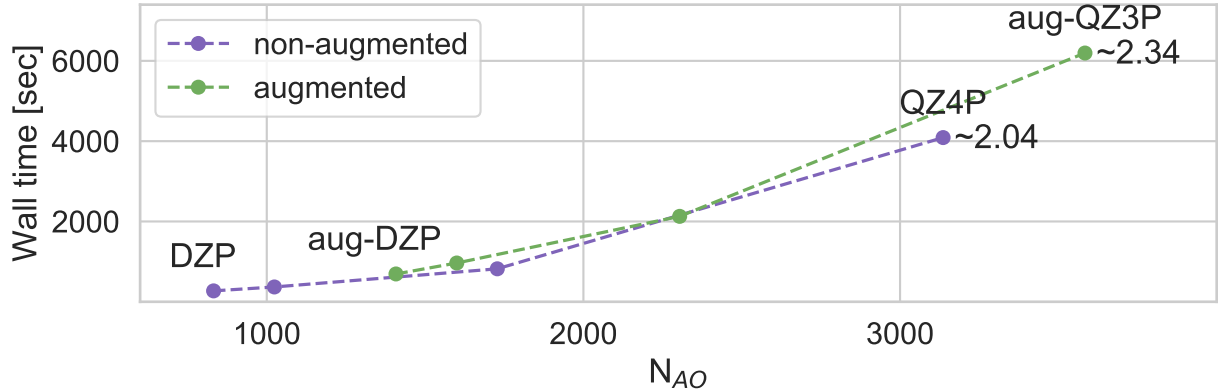


Figure 9: Timings (in seconds) and asymptotic scaling of our algorithm with basis sets of increasing size for $(\text{H}_2\text{O})_{32}$ with the same settings as described above (*Normal* thresholds) using a single bw node.

Next, we investigate scaling with respect to the single-particle basis at fixed systems size. As shown in figure 9, even for the small $(\text{H}_2\text{O})_{32}$ cluster, our algorithm scales quadratic with the size of the single-particle basis when non-augmented basis sets are used. Using augmented basis sets, the asymptotic scaling is worse owing to the large number of basis functions with a very slow decay with the distance to the nuclei on which they are centred, leading to a smaller number of negligible AO-products. High scaling with respect to the single-particle basis is a general shortcoming of AO-based algorithms compared to MO-based ones and its current form it is difficult to envisage modifications of our algorithm which might overcome this issue.

Finally, we comment on the parallel performance of our algorithm. Figure 10 shows the speed-up with increasing number of cores. We achieve a parallel efficiency of 66 % when going from 1 to 24 cores. The deviation to the ideal speed-up is partly due to small fractions of serial code in our algorithm but also due to unnecessary network communication. Also due to the latter factor, parallelization over multiple nodes is less efficient. At the moment, our algorithms for the calculation of P and Σ communicate a lot of data, an aspect which we have not optimized yet.

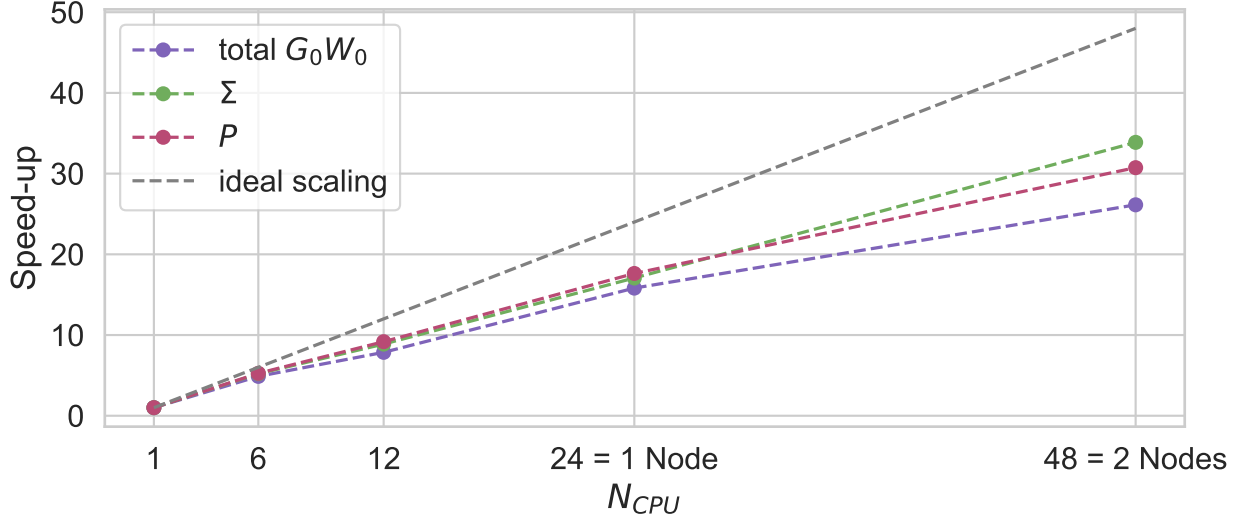


Figure 10: Speed-up for $(\text{H}_2\text{O})_{64}$ (same settings as described above, *Normal* thresholds) with the number of CPUs.

For completeness, we also mention the large memory count of our algorithm increasing as N^2 with systems size. However, the practical memory bottleneck is rather the storage of C . Although only linearly scaling, we store it in shared memory which prevents the scalability of our algorithm to even larger systems. The memory requirements are reduced for low-dimensional systems for which C becomes smaller, however, it is clear that systems much larger than the ones presented herein can not be treated any more. Still, for systems of hundreds of atoms for which conventional implementations require a supercomputer,^{98,99} G_0W_0 calculations with our algorithm can be performed in a routine fashion which puts its application in main-stream computational spectroscopy within reach.

4 Conclusion

In this work, we have presented a PADF-based G_0W_0 implementation using STOs and relying on imaginary time-representation of the single-particle Green’s function. Our algorithm combines quadratic scaling in memory and operation count with a very small prefactor due to a sparse map from ABF space to AO-product space. Using realistic numerical settings,

a G_0W_0 calculation for a spherically shaped water cluster with 432 atoms, 7776 AOs, and 36576 ABFs takes 240 CPU hours. Using slightly looser thresholds, the same calculation is done in 180 CPU hours and the G_0W_0 calculations for a linear alkane chain with the same number of AOs takes only about 100 CPU hours. Thus, our algorithm is at least one order of magnitude faster than the fastest state-of-the-art canonical implementations.^{99,209}

The accuracy of our algorithm for the calculation of the HOMO and LUMO QP energies in the GW100 database has been investigated by comparison to RS-CBSLE reference values. We found MADs of 0.38 eV for TZ2P and 0.26 eV for QZ4P for the HOMO, and 0.93 eV for TZ2P and 0.55 eV for QZ4P for the LUMO energies, respectively. For the HOMO level, FHI-AIMS/def2-QZVP only deviates from the CBS limit by 0.15 eV on average and TURBOMOLE/TZVP by 0.28 eV. Thus, for GW100, the accuracy of our algorithm on the QZ level is comparable to canonical implementations on the TZ level while it is difficult to make a definite statement about the quality of our LUMO energies due to large discrepancies between different codes.^{82,210,226,227}

Two factors contribute to the relatively poor performance of our algorithm for GW100. First, for many systems with QP solutions close to poles of the self-energy, our frequency treatment with AC is inaccurate and we often observe large differences with respect to the reference. This feature is also observed within other closely related schemes.^{99,226} As expected,²¹⁰ this issue is mostly avoided when a gKS reference is used. Certainly, using a more sophisticated algorithm to generate larger imaginary frequency grids than the present ones which are limited to a maximum of 19 points will also improve our algorithm for systems with a small KS HOMO-LUMO gap and/or low-lying core states for which generally higher resolution on the frequency axes is required.²³⁷

Second, the PADF-approach becomes numerical unstable for large basis sets. To restore numerical stability, parts of the unoccupied space needs to be projected out during the SCF which effectively diminishes the size of the basis, especially when the basis set comprises many diffuse functions. This shortcoming can be traced back to the intrinsic difficulty to

represent highly delocalized AO-pair densities using ABFs centered on two atoms only. With our auxiliary fit sets having been optimized for gKS calculations, this can lead to very large fitting coefficients which in turn cause numerical instabilities. This issue is of technical nature and can possibly be resolved by adding more diffuse functions with high angular momenta to our current auxiliary basis sets.¹⁶⁰ Employing auxiliary basis sets optimized for correlated methods, as it is common practice in global DF,^{238–244} seems to be a promising route to approach the accuracy of canonical G_0W_0 also for large QZ basis sets and large systems.

Using smaller basis sets of augmented DZ and TZ quality, we calculated the HOMO and LUMO energies of a set of 250 organic molecules between 12 and 99 atoms from the GW5000 database and observed that the deviation to the FHI-AIMS CBSLE reference, not only within our scheme but also within the canonical scheme using GTO-type basis sets, is actually decreasing with increasing system size. Thus, we conclude that PADF- G_0W_0 calculations on the augmented DZ and TZ level can safely be performed for large systems as well. For another subset of GW5000 comprising 20 large molecules with in between 85 and 99 atoms, the aug-DZP HOMO-LUMO gap deviates by only 0.08 eV on average from the CBS limit, which is comparable to the FHI-AIMS/def-TZVP reference.

To summarize, it is clear that further technical improvements of our algorithm are needed. Nevertheless, the examples in this work demonstrate that already in its current form it enables accurate G_0W_0 calculations for large systems of hundreds of atoms with TZ and augmented DZ basis sets in a routine fashion. Not only its scalability, but also its very small prefactor make it amenable to quasi-particle and fully self-consistent GW calculations which are possible with straightforward extensions of our algorithm since we construct the complete Σ instead of only its diagonal in the MO basis. Due to the usually consistent overestimation of QP energies, BSEs often compensate each other to a large extend in calculations of HOMO-LUMO gaps and in the past many GW calculations with augmented DZ basis sets have provided important insights into the electronic properties of practically relevant systems.^{73,209,232–235} This indicates, that our algorithm might prove useful in practice already in

its current form e.g. in the study of large organic chromophores in solution or donor-acceptor systems, and we think that its computational efficiency out-weights its current limitations to reach the CBS limit with guaranteed accuracy.

Acknowledgement

This research received funding from the Netherlands Organisation for Scientific Research (NWO) in the framework of the Innovation Fund for Chemistry and from the Ministry of Economic Affairs in the framework of the “*TKI/PPS-Toeslagregeling*”.

Supporting Information Available

The following files are available free of charge.

- i) All calculated QP HOMO and LUMO energies for the GW100 and the subsets of the GW5000 database and fit-parameters for figure 6 and additional plots.
- ii) Explicit values for thresholds controlling distance effects as well as some explanations.
- iii) .txt-file with imaginary frequency grids for some orbital energy ranges serving as starting values for our Levenberg-Marquardt algorithm as well as corresponding errors of the approximate quadratures of the MP2 energy denominator.

References

- (1) Jensen, P.; Bunker, P. R. *Computational molecular spectroscopy*; Wiley, 2000.
- (2) Parson, W. W. *Modern Optical Spectroscopy*; Springer, Berlin Heidelberg, 2007.

(3) Martin-Drumel, M. A.; McCarthy, M. C.; Patterson, D.; McGuire, B. A.; Crabtree, K. N. Automated microwave double resonance spectroscopy: A tool to identify and characterize chemical compounds. *J. Chem. Phys.* **2016**, *144*, 124202.

(4) Sugiki, T.; Kobayashi, N.; Fujiwara, T. Modern Technologies of Solution Nuclear Magnetic Resonance Spectroscopy for Three-dimensional Structure Determination of Proteins Open Avenues for Life Scientists. *Comput. Struct. Biotechnol. J.* **2017**, *15*, 328–339.

(5) Puzzarini, C.; Barone, V. Diving for Accurate Structures in the Ocean of Molecular Systems with the Help of Spectroscopy and Quantum Chemistry. *Acc. Chem. Res.* **2018**, *51*, 548–556.

(6) Choi, J. H.; Lee, H.; Lee, K. K.; Hahn, S.; Cho, M. Computational spectroscopy of ubiquitin: Comparison between theory and experiments. *J. Chem. Phys.* **2007**, *126*, 045102.

(7) Boukhvalov, D. W.; Katsnelson, M. I. Modeling of graphite oxide. *J. Am. Chem. Soc.* **2008**, *130*, 10697–10701.

(8) Zhang, W.; Caravetta, V.; Li, Z.; Luo, Y.; Yang, J. Oxidation states of graphene: Insights from computational spectroscopy. *J. Chem. Phys.* **2009**, *131*, 244505.

(9) Pedone, A.; Biczysko, M.; Barone, V. Environmental effects in computational spectroscopy: Accuracy and interpretation. *ChemPhysChem* **2010**, *11*, 1812–1832.

(10) Puzzarini, C.; Stanton, J. F.; Gauss, J. Quantum-chemical calculation of spectroscopic parameters for rotational spectroscopy. *Int. Rev. Phys. Chem.* **2010**, *29*, 273–367.

(11) Barone, V. *Computational strategies for spectroscopy: from small molecules to nano systems*; John Wiley & Sons, 2011.

(12) Berova, N.; Polavarapu, P. L.; Nakanishi, K.; Woody, R. W. *Comprehensive Chiroptical Spectroscopy: Instrumentation, Methodologies, and Theoretical Simulations*, 1st ed.; John Wiley & Sons, 2011.

(13) Barone, V.; Baiardi, A.; Biczysko, M.; Bloino, J.; Cappelli, C.; Lipparini, F. Implementation and validation of a multi-purpose virtual spectrometer for large systems in complex environments. *Phys. Chem. Chem. Phys.* **2012**, *14*, 12404–12422.

(14) Kessler, J.; Andrushchenko, V.; Kapitán, J.; Bou, P. Insight into vibrational circular dichroism of proteins by density functional modeling. *Phys. Chem. Chem. Phys.* **2018**, *20*, 4926–4935.

(15) Puzzarini, C.; Bloino, J.; Tasinato, N.; Barone, V. Accuracy and Interpretability: The Devil and the Holy Grail. New Routes across Old Boundaries in Computational Spectroscopy. *Chem. Rev.* **2019**, *119*, 8131–8191.

(16) Kohn, W.; Sham. L. J., Self-Consistent Equations Including Exchange and Correlation Effects. *Phys. Rev.* **1965**, *140*, A1133.

(17) Hohenberg, P.; Kohn, W. Inhomogeneous Electron Gas. *Phys. Rev.* **1964**, *136*, 864–871.

(18) Levy, M. Universal variational functionals of electron densities, first-order density matrices, and natural spin-orbitals and solution of the v-representability problem. *Physics (College. Park. Md.)*. **1979**, *76*, 6062–6065.

(19) Engel, E.; Dreizler, R. M. *Density Functional Theory: An Advanced Course*; Springer, 2013.

(20) Hickey, A. L.; Rowley, C. N. Benchmarking quantum chemical methods for the calculation of molecular dipole moments and polarizabilities. *J. Phys. Chem. A* **2014**, *118*, 3678–3687.

(21) Becke, A. D. Perspective: Fifty years of density-functional theory in chemical physics. *J. Chem. Phys.* **2014**, *140*, 18A301.

(22) Pribram-Jones, A.; Gross, D. A.; Burke, K. DFT: A Theory Full of Holes? *Annu. Rev. Phys. Chem.* **2015**, *66*, 283–304.

(23) Yu, H. S.; Li, S. L.; Truhlar, D. G. Perspective: Kohn-Sham density functional theory descending a staircase. *J. Chem. Phys.* **2016**, *145*, 130901.

(24) Goerigk, L.; Hansen, A.; Bauer, C.; Ehrlich, S.; Najibi, A.; Grimme, S. A look at the density functional theory zoo with the advanced GMTKN55 database for general main group thermochemistry, kinetics and noncovalent interactions. *Phys. Chem. Chem. Phys.* **2017**, *19*, 32184–32215.

(25) Mardirossian, N.; Head-Gordon, M. Thirty years of density functional theory in computational chemistry: An overview and extensive assessment of 200 density functionals. *Mol. Phys.* **2017**, *115*, 2315–2372.

(26) Grimme, S.; Schreiner, P. R. Computational Chemistry: The Fate of Current Methods and Future Challenges. *Angew. Chemie - Int. Ed.* **2018**, *57*, 4170–4176.

(27) Godby, R. W.; Schlüter, M.; Sham, L. J. Self-energy operators and exchange-correlation potentials in semiconductors. *Phys. Rev. B* **1988**, *37*, 10159–10175.

(28) Engel, E.; Chevary, J. A.; Macdonald, L. D.; Vosko, S. H. Asymptotic properties of the exchange energy density and the exchange potential of finite systems: relevance for generalized gradient approximations. *Zeitschrift für Phys. D Atoms, Mol. Clust.* **1992**, *23*, 7–14.

(29) Steinbeck, L.; Rubio, A.; Reining, L.; Torrent, M.; White, I. D.; Godby, R. W. Enhancements to the GW space-time method. *Comput. Phys. Commun.* **2000**, *125*, 105–118.

(30) Grünig, M.; Gritsenko, O. V.; Van Gisbergen, S. J.; Jan Baerends, E. On the required shape corrections to the local density and generalized gradient approximations to the Kohn-Sham potentials for molecular response calculations of (hyper)polarizabilities and excitation energies. *J. Chem. Phys.* **2002**, *116*, 9591–9601.

(31) Grünig, M.; Gritsenko, O. V.; Baerends, E. J. Exchange potential from the common energy denominator approximation for the Kohn-Sham Green's function: Application to (hyper)polarizabilities of molecular chains. *J. Chem. Phys.* **2002**, *116*, 6435–6442.

(32) Malet, F.; Gori-Giorgi, P. Strong correlation in Kohn-Sham density functional theory. *Phys. Rev. Lett.* **2012**, *109*, 1–5.

(33) Baerends, E. J.; Gritsenko, O. V.; Van Meer, R. The Kohn-Sham gap, the fundamental gap and the optical gap: The physical meaning of occupied and virtual Kohn-Sham orbital energies. *Phys. Chem. Chem. Phys.* **2013**, *15*, 16408–16425.

(34) Van Meer, R.; Gritsenko, O. V.; Baerends, E. J. Physical meaning of virtual kohn-sham orbitals and orbital energies: An ideal basis for the description of molecular excitations. *J. Chem. Theory Comput.* **2014**, *10*, 4432–4441.

(35) Gritsenko, O. V.; Mentel, M.; Baerends, E. J. On the errors of local density (LDA) and generalized gradient (GGA) approximations to the Kohn-Sham potential and orbital energies. *J. Chem. Phys.* **2016**, *144*, 204114.

(36) Baerends, E. J. From the Kohn-Sham band gap to the fundamental gap in solids. An integer electron approach. *Phys. Chem. Chem. Phys.* **2017**, *19*, 15639–15656.

(37) Thygesen, K. S.; Rubio, A. Nonequilibrium GW approach to quantum transport in nano-scale contacts. *J. Chem. Phys.* **2007**, *126*, 091101.

(38) Darancet, P.; Ferretti, A.; Mayou, D.; Olevano, V. Ab initio GW electron-electron interaction effects in Quantum Transport. *Phys. Rev. B* **2017**, *75*, 075102.

(39) Thoss, M.; Evers, F. Perspective : Theory of quantum transport in molecular junctions. *J. Chem. Phys.* **2018**, *148*, 030901.

(40) Unjić, M.; Maruić, L. Dynamical effects in electron tunneling: Self-consistent semi-classical image potentials. *Phys. Rev. B* **1991**, *44*, 9092–9095.

(41) Rignanese, G. M.; Blase, X.; Louie, S. G. Quasiparticle effects on tunneling currents: A study of C₂H₄ adsorbed on the Si(001)-(2 X 1) surface. *Phys. Rev. Lett.* **2001**, *86*, 2110–2113.

(42) Dial, O. E.; Ashoori, R. C.; Pfeiffer, L. N.; West, K. W. Observations of plasmarons in a two-dimensional system: Tunneling measurements using time-domain capacitance spectroscopy. *Phys. Rev. B* **2012**, *85*, 081306.

(43) Aryasetiawan, F.; Gunnarsson, O. The GW method. *Reports Prog. Phys.* **1998**, *61*, 237–312.

(44) Lischner, J.; Vigil-Fowler, D.; Louie, S. G. Physical origin of satellites in photoemission of doped graphene: An Ab initio GW plus cumulant study. *Phys. Rev. Lett.* **2013**, *110*, 146801.

(45) Golze, D.; Wilhelm, J.; Van Setten, M. J.; Rinke, P. Core-Level Binding Energies from GW: An Efficient Full-Frequency Approach within a Localized Basis. *J. Chem. Theory Comput.* **2018**, *14*, 4856–4869.

(46) Golze, D.; Dvorak, M.; Rinke, P. The GW Compendium: A Practical Guide to Theoretical Photoemission Spectroscopy. *Front. Chem.* **2019**, *7*, 377.

(47) Golze, D.; Keller, L.; Rinke, P. Accurate Absolute and Relative Core-Level Binding Energies From GW. *J. Phys. Chem. Lett.* **2020**, *11*, 1840–1847.

(48) Kühne, T. D.; Iannuzzi, M.; Del Ben, M.; Rybkin, V. V.; Seewald, P.; Stein, F.; Laino, T.; Khaliullin, R. Z.; Schütt, O.; Schiffmann, F.; Golze, D.; Wilhelm, J.;

Chulkov, S.; Bani-Hashemian, M. H.; Weber, V.; Borstnik, U.; Taillefumier, M.; Jakobovits, A. S.; Lazzaro, A.; Pabst, H.; Müller, T.; Schade, R.; Guidon, M.; Andermatt, S.; Holmberg, N.; Schenter, G. K.; Hehn, A.; Bussy, A.; Belleflamme, F.; Tabacchi, G.; Glöß, A.; Lass, M.; Bethune, I.; Mundy, C. J.; Plessl, C.; Watkins, M.; VandeVondele, J.; Krack, M.; Hutter, J. CP2K: An Electronic Structure and Molecular Dynamics Software Package – Quickstep: Efficient and Accurate Electronic Structure Calculations. *J. Chem. Phys.* **2020**, *152*, 194103.

(49) Luttinger, J. M.; Ward, J. C. On correlation effects in electron spectroscopies and the GW approximation. *Phys. Rev.* **1960**, *118*, 1417.

(50) Baym, G.; Kadanoff, L. P. Conservation laws and correlation functions. *Phys. Rev.* **1961**, *124*, 287–299.

(51) Hedin, L. New method for calculating the one-particle Green's function with application to the electron-gas problem. *Phys. Rev.* **1965**, *139*, A796.

(52) Onida, G.; Nazionale, I.; Vergata, R. T.; Scientifica, R.; Roma, I. Electronic excitations: density-functional versus many-body Green's-function approaches. *Rev. Mod. Phys.* **2002**, *74*, 601.

(53) Martin, R. M.; Reining, L.; Ceperley, D. M. *Interacting electrons*; Cambridge University Press, 2016.

(54) Reining, L. The GW approximation: content, successes and limitations. *Wiley Interdiscip. Rev. Comput. Mol. Sci.* **2018**, *8*, e1344.

(55) Hybertsen, M. S.; Louie, S. G. Electron correlation in semiconductors and insulators: Band gaps and quasiparticle energies. *Phys. Rev. B* **1986**, *34*, 5390.

(56) Deslippe, J.; Samsonidze, G.; Strubbe, D. A.; Jain, M.; Cohen, M. L.; Louie, S. G. BerkeleyGW: A massively parallel computer package for the calculation of the quasi-

particle and optical properties of materials and nanostructures. *Comput. Phys. Commun.* **2012**, *183*, 1269–1289.

(57) Pavlyukh, Y.; Stefanucci, G.; van Leeuwen, R. Dynamically screened vertex correction to GW. *Arxiv:2004.05344* **2020**,

(58) Knight, J. W.; Wang, X.; Gallandi, L.; Dolgounitcheva, O.; Ren, X.; Ortiz, J. V.; Rinke, P.; Körzdörfer, T.; Marom, N. Accurate Ionization Potentials and Electron Affinities of Acceptor Molecules III: A Benchmark of GW Methods. *J. Chem. Theory Comput.* **2016**, *12*, 615–626.

(59) Salpeter, E. E.; Bethe, H. A. A relativistic equation for bound-state problems. *Phys. Rev.* **1951**, *84*, 1232–1242.

(60) Strinati, G. Application of the Green's functions method to the study of the optical properties of semiconductors. *La Riv. Del Nuovo Cim. Ser. 3* **1988**, *11*, 1–86.

(61) Gonze, X.; Beuken, J. M.; Caracas, R.; Detraux, F.; Fuchs, M.; Rignanese, G. M.; Sindic, L.; Verstraete, M.; Zerah, G.; Jollet, F.; Torrent, M.; Roy, A.; Mikami, M.; Ghosez, P.; Raty, J. Y.; Allan, D. C. First-principles computation of material properties: The ABINIT software project. *Comput. Mater. Sci.* **2002**, *25*, 478–492.

(62) Gonze, X.; Amadon, B.; Anglade, P. M.; Beuken, J. M.; Bottin, F.; Boulanger, P.; Bruneval, F.; Caliste, D.; Caracas, R.; Côté, M.; Deutsch, T.; Genovese, L.; Ghosez, P.; Giantomassi, M.; Goedecker, S.; Hamann, D. R.; Hermet, P.; Jollet, F.; Jomard, G.; Leroux, S.; Mancini, M.; Mazevert, S.; Oliveira, M. J.; Onida, G.; Pouillon, Y.; Rangel, T.; Rignanese, G. M.; Sangalli, D.; Shaltaf, R.; Torrent, M.; Verstraete, M. J.; Zerah, G.; Zwanziger, J. W. ABINIT: First-principles approach to material and nanosystem properties. *Comput. Phys. Commun.* **2009**, *180*, 2582–2615.

(63) Nguyen, H. V.; Pham, T. A.; Rocca, D.; Galli, G. Improving accuracy and efficiency

of calculations of photoemission spectra within the many-body perturbation theory. *Phys. Rev. B* **2012**, *85*, 081101.

- (64) Pham, T. A.; Nguyen, H. V.; Rocca, D.; Galli, G. GW calculations using the spectral decomposition of the dielectric matrix: Verification, validation, and comparison of methods. *Phys. Rev. B* **2013**, *87*, 1–12.
- (65) Kresse, G.; Furthmüller, J. Efficient iterative schemes for ab initio total-energy calculations using a plane-wave basis set. *Phys. Rev. B* **1996**, *54*, 11169–11186.
- (66) Kresse, G.; Furthmüller, J. Efficiency of ab-initio total energy calculations for metals and semiconductors using a plane-wave basis set. *Comput. Mater. Sci.* **1996**, *6*, 15–50.
- (67) Joubert, D. From ultrasoft pseudopotentials to the projector augmented-wave method. *Phys. Rev. B* **1999**, *59*, 1758–1775.
- (68) Blum, V.; Gehrke, R.; Hanke, F.; Havu, P.; Havu, V.; Ren, X.; Reuter, K.; Scheffler, M. The Fritz Haber Institute ab initio molecular simulations package (FHI-aims), <http://www.fhi-berlin.mpg.de/aims>, 2009.
- (69) Blum, V.; Gehrke, R.; Hanke, F.; Havu, P.; Havu, V.; Ren, X.; Reuter, K.; Scheffler, M. Ab initio molecular simulations with numeric atom-centered orbitals. *Comput. Phys. Commun.* **2009**, *180*, 2175–2196.
- (70) Bruneval, F.; Rangel, T.; Hamed, S. M.; Shao, M.; Yang, C.; Neaton, J. B. MOLGW 1: Many-body perturbation theory software for atoms, molecules, and clusters. *Comput. Phys. Commun.* **2016**, *208*, 149–161.
- (71) Sangalli, D.; Ferretti, A.; Miranda, H.; Attaccalite, C.; Marri, I.; Cannuccia, E.; Melo, P.; Marsili, M.; Paleari, F.; Marrazzo, A.; Prandini, G.; Bonfà, P.; Atambo, M. O.; Affinito, F.; Palummo, M.; Molina-Sánchez, A.; Hogan, C.;

Grünig, M.; Varsano, D.; Marini, A. Many-body perturbation theory calculations using the yambo code. *J. Phys. Condens. Matter* **2019**, *31*, 325902.

(72) Schlipf, M.; Lambert, H.; Zibouche, N.; Giustino, F. STERNHEIMERGW: A program for calculating GW quasiparticle band structures and spectral functions without unoccupied states. *Comput. Phys. Commun.* **2020**, *247*, 106856.

(73) Blase, X.; Attaccalite, C.; Olevano, V. First-principles GW calculations for fullerenes, porphyrins, phtalocyanine, and other molecules of interest for organic photovoltaic applications. *Phys. Rev. B* **2011**, *83*, 1–9.

(74) Faber, C.; Attaccalite, C.; Olevano, V.; Runge, E.; Blase, X. First-principles GW calculations for DNA and RNA nucleobases. *Phys. Rev. B* **2011**, *81*, 115123.

(75) Strange, M.; Rostgaard, C.; Häkkinen, H.; Thygesen, K. S. Self-consistent GW calculations of electronic transport in thiol- and amine-linked molecular junctions. *Phys. Rev. B* **2011**, *83*, 1–12.

(76) Marom, N.; Caruso, F.; Ren, X.; Hofmann, O. T.; Körzdörfer, T.; Chelikowsky, J. R.; Rubio, A.; Scheffler, M.; Rinke, P. Benchmark of GW methods for azabenzenes. *Phys. Rev. B* **2012**, *86*, 1–16.

(77) Baumeier, B.; Andrienko, D.; Rohlfing, M. Frenkel and charge-transfer excitations in donor-acceptor complexes from many-body green's functions theory. *J. Chem. Theory Comput.* **2012**, *8*, 2790–2795.

(78) Bruneval, F.; Marques, M. A. Benchmarking the starting points of the GW approximation for molecules. *J. Chem. Theory Comput.* **2013**, *9*, 324–329.

(79) Caruso, F.; Rohr, D. R.; Hellgren, M.; Ren, X.; Rinke, P.; Rubio, A.; Scheffler, M. Bond breaking and bond formation: How electron correlation is captured in many-

body perturbation theory and density-functional theory. *Phys. Rev. Lett.* **2013**, *110*, 1–5.

(80) Faber, C.; Boulanger, P.; Duchemin, I.; Attaccalite, C.; Blase, X. Many-body Green's function GW and Bethe-Salpeter study of the optical excitations in a paradigmatic model dipeptide. *J. Chem. Phys.* **2013**, *139*, 194308.

(81) Körbel, S.; Boulanger, P.; Duchemin, I.; Blase, X.; Marques, M. A.; Botti, S. Benchmark many-body GW and Bethe-Salpeter calculations for small transition metal molecules. *J. Chem. Theory Comput.* **2014**, *10*, 3934–3943.

(82) Van Setten, M. J.; Caruso, F.; Sharifzadeh, S.; Ren, X.; Scheffler, M.; Liu, F.; Lischner, J.; Lin, L.; Deslippe, J. R.; Louie, S. G.; Yang, C.; Weigend, F.; Neaton, J. B.; Evers, F.; Rinke, P. GW100: Benchmarking G0W0 for Molecular Systems. *J. Chem. Theory Comput.* **2015**, *11*, 5665–5687.

(83) Rangel, T.; Hamed, S. M.; Bruneval, F.; Neaton, J. B. Evaluating the GW Approximation with CCSD(T) for Charged Excitations Across the Oligoacenes. *J. Chem. Theory Comput.* **2016**, *12*, 2834–2842.

(84) Li, J.; D'Avino, G.; Duchemin, I.; Beljonne, D.; Blase, X. Combining the Many-Body GW Formalism with Classical Polarizable Models: Insights on the Electronic Structure of Molecular Solids. *J. Phys. Chem. Lett.* **2016**, *7*, 2814–2820.

(85) Duchemin, I.; Jacquemin, D.; Blase, X. Combining the GW formalism with the polarizable continuum model: A state-specific non-equilibrium approach. *J. Chem. Phys.* **2016**, *144*, 164106.

(86) Scherpelz, P.; Govoni, M.; Hamada, I.; Galli, G. Implementation and Validation of Fully Relativistic GW Calculations: Spin-Orbit Coupling in Molecules, Nanocrystals, and Solids. *J. Chem. Theory Comput.* **2016**, *12*, 3523–3544.

(87) Maggio, E.; Kresse, G. GW Vertex Corrected Calculations for Molecular Systems. *J. Chem. Theory Comput.* **2017**, *13*, 4765–4778.

(88) Hung, L.; Bruneval, F.; Baishya, K.; Öüt, S. Benchmarking the GW Approximation and Bethe-Salpeter Equation for Groups IB and IIB Atoms and Monoxides. *J. Chem. Theory Comput.* **2017**, *13*, 2135–2146.

(89) Olsen, T.; Patrick, C. E.; Bates, J. E.; Ruzsinszky, A.; Thygesen, K. S. Beyond the RPA and GW methods with adiabatic xc-kernels for accurate ground state and quasi-particle energies. *Nat. Comput. Mater.* **2019**, *5*, 106.

(90) Bruneval, F. Assessment of the Linearized GW Density Matrix for Molecules. *J. Chem. Theory Comput.* **2019**, *15*, 4069–4078.

(91) Lewis, A. M.; Berkelbach, T. C. Vertex Corrections to the Polarizability Do Not Improve the GW Approximation for the Ionization Potential of Molecules. *J. Chem. Theory Comput.* **2019**, *15*, 2925–2932.

(92) Holzer, C.; Klopper, W. Ionized, electron-attached, and excited states of molecular systems with spin-orbit coupling: Two-component GW and Bethe-Salpeter implementations. *J. Chem. Phys.* **2019**, *150*, 204116.

(93) Cazzaniga, M.; Cagnoni, F.; Penconi, M.; Bossi, A.; Ceresoli, D. Ab Initio Many-Body Perturbation Theory Calculations of the Electronic and Optical Properties of Cyclometalated Ir(III) Complexes. *J. Chem. Theory Comput.* **2020**, *16*, 1188–1199.

(94) Caruso, F.; Dauth, M.; Van Setten, M. J.; Rinke, P. Benchmark of GW Approaches for the GW100 Test Set. *J. Chem. Theory Comput.* **2016**, *12*, 5076–5087.

(95) The notion of N^x always implies $\mathcal{O}(N^x)$: That is, the function f , mapping the system size to the run-time of an algorithm, does asymptotically not grow faster than N^x .

(96) Shih, B. C.; Xue, Y.; Zhang, P.; Cohen, M. L.; Louie, S. G. Quasiparticle band gap of ZnO: High accuracy from the conventional G0W0 approach. *Phys. Rev. Lett.* **2010**, *105*, 1–4.

(97) Nguyen, H. V.; Pham, T. A.; Rocca, D.; Galli, G. Improving accuracy and efficiency of calculations of photoemission spectra within the many-body perturbation theory. *Phys. Rev. B* **2012**, *85*, 1–5.

(98) Del Ben, M.; da Jornada, F. H.; Canning, A.; Wichmann, N.; Raman, K.; Sasanka, R.; Yang, C.; Louie, S. G.; Deslippe, J. Large-scale GW calculations on pre-exascale HPC systems. *Comput. Phys. Commun.* **2019**, *235*, 187–195.

(99) Wilhelm, J.; Golze, D.; Talirz, L.; Hutter, J.; Pignedoli, C. A. Toward GW Calculations on Thousands of Atoms. *J. Phys. Chem. Lett.* **2018**, *9*, 306–312.

(100) Neuhauser, D.; Gao, Y.; Arntsen, C.; Karshenas, C.; Rabani, E.; Baer, R. Breaking the theoretical scaling limit for predicting quasiparticle energies: The stochastic GW approach. *Phys. Rev. Lett.* **2014**, *113*, 1–5.

(101) Vlček, V.; Rabani, E.; Neuhauser, D.; Baer, R. Stochastic GW Calculations for Molecules. *J. Chem. Theory Comput.* **2017**, *13*, 4997–5003.

(102) Vlček, V.; Li, W.; Baer, R.; Rabani, E.; Neuhauser, D. Swift GW beyond 10,000 electrons using sparse stochastic compression. *Phys. Rev. B* **2018**, *98*, 0–10.

(103) Umari, P.; Stenuit, G.; Baroni, S. GW quasiparticle spectra from occupied states only. *Phys. Rev. B* **2010**, *81*, 1–5.

(104) Giustino, F.; Cohen, M. L.; Louie, S. G. GW method with the self-consistent Sternheimer equation. *Phys. Rev. B* **2010**, *81*, 1–18.

(105) Lambert, H.; Giustino, F. Ab initio Sternheimer-GW method for quasiparticle calculations using plane waves. *Phys. Rev. B* **2013**, *88*, 1–13.

(106) Bruneval, F. Optimized virtual orbital subspace for faster GW calculations in localized basis. *J. Chem. Phys.* **2016**, *145*, 234110.

(107) Govoni, M.; Galli, G. Large Scale GW Calculations. *J. Chem. Theory Comput.* **2015**, *11*, 2680–2696.

(108) Rostgaard, C.; Jacobsen, K. W.; Thygesen, K. S. Fully self-consistent GW calculations for molecules. *Phys. Rev. B* **2010**, *81*, 1–10.

(109) Shao, M. Y.; Lin, L.; Yang, C.; Liu, F.; Da Jornada, F. H.; Deslippe, J.; Louie, S. G. Low rank approximation in G0W0 calculations. *Sci. China Math.* **2016**, *59*, 1593–1612.

(110) Klimeš, J.; Kaltak, M.; Kresse, G. Predictive GW calculations using plane waves and pseudopotentials. *Phys. Rev. B* **2014**, *90*, 1–15.

(111) Riemelmoser, S.; Kaltak, M.; Kresse, G. Plane wave basis set correction methods for RPA correlation energies. *J. Chem. Phys.* **2020**, *152*, 1–13.

(112) Loos, P. F.; Pradines, B.; Scemama, A.; Giner, E.; Toulouse, J. Density-Based Basis-Set Incompleteness Correction for GW Methods. *J. Chem. Theory Comput.* **2020**, *16*, 1018–1028.

(113) Helgaker, T.; Jorgensen, P.; Olsen, J. *Molecular electronic-structure theory*; John Wiley & Sons, 2014.

(114) Billingsley, F. P.; Bloor, J. E. Limited expansion of diatomic overlap (LEDO): A Near-accurate approximate Ab Initio LCAO MO Method. I. Theory and preliminary investigations. *J. Chem. Phys.* **1971**, *55*, 5178–5190.

(115) Baerends, E. J.; Ellis, D. E.; Ros, P. Self-consistent molecular HartreeFockSlater calculations I. The computational procedure. *Chem. Phys.* **1973**, *2*, 41–51.

(116) Whitten, J. L. Coulombic potential energy integrals and approximations. *J. Chem. Phys.* **1973**, *58*, 4496–4501.

(117) Sambe, H.; Felton, R. H. A new computational approach to Slater's SCF-X α equation. *J. Chem. Phys.* **1975**, *62*, 1122–1126.

(118) Dunlap, B. I.; Connolly, J. W.; Sabin, J. R. On some approximations in applications of X α theory. *J. Chem. Phys.* **1979**, *71*, 3396–3402.

(119) Dunlap, B. I.; Connolly, J. W.; Sabin, J. R. On first-row diatomic molecules and local density models. *J. Chem. Phys.* **1979**, *71*, 4993–4999.

(120) Vahtras, O.; Almlöf, J.; Feyereisen, M. W. Integral approximations for LCAO-SCF calculations. *Chem. Phys. Lett.* **1993**, *213*, 514–518.

(121) Feyereisen, M.; Fitzgerald, G.; Komornicki, A. Use of approximate integrals in ab initio theory. An application in MP2 energy calculations. *Chem. Phys. Lett.* **1993**, *208*, 359–363.

(122) Kendall, R. A.; Früchtl, H. A. The impact of the resolution of the identity approximate integral method on modern ab initio algorithm development. *Theor. Chem. Acc.* **1997**, *97*, 158–163.

(123) Dunlap, B. I. Robust and variational fitting: Removing the four-center integrals from center stage in quantum chemistry. *J. Mol. Struct. THEOCHEM* **2000**, *529*, 37–40.

(124) Dunlap, B. I. Robust and variational fitting. *Phys. Chem. Chem. Phys.* **2000**, *2*, 2113–2116.

(125) Weigend, F. Accurate Coulomb-fitting basis sets for H to Rn. *Phys. Chem. Chem. Phys.* **2006**, *8*, 1057–1065.

(126) Dunlap, B. I.; Rösch, N.; Trickey, S. B. Variational fitting methods for electronic structure calculations. *Mol. Phys.* **2010**, *108*, 3167–3180.

(127) Beebe, N. H.; Linderberg, J. Simplifications in the generation and transformation of twoelectron integrals in molecular calculations. *Int. J. Quantum Chem.* **1977**, *12*, 683–705.

(128) Koch, H.; Sánchez De Merás, A.; Pedersen, T. B. Reduced scaling in electronic structure calculations using Cholesky decompositions. *J. Chem. Phys.* **2003**, *118*, 9481–9484.

(129) Aquilante, F.; Lindh, R.; Bondo Pedersen, T. Unbiased auxiliary basis sets for accurate two-electron integral approximations. *J. Chem. Phys.* **2007**, *127*, 114107.

(130) Boman, L.; Koch, H.; Sánchez De Merás, A. Method specific Cholesky decomposition: Coulomb and exchange energies. *J. Chem. Phys.* **2008**, *129*, 134107.

(131) Aquilante, F.; Gagliardi, L.; Pedersen, T. B.; Lindh, R. Atomic Cholesky decompositions: A route to unbiased auxiliary basis sets for density fitting approximation with tunable accuracy and efficiency. *J. Chem. Phys.* **2009**, *130*, 154107.

(132) Foerster, D.; Koval, P.; Snchez-Portal, D. An O(N3) implementation of Hedin's GW approximation for molecules. *J. Chem. Phys.* **2011**, *135*, 074105.

(133) Ke, S. H. All-electron GW methods implemented in molecular orbital space: Ionization energy and electron affinity of conjugated molecules. *Phys. Rev. B* **2011**, *84*, 4–7.

(134) Ren, X.; Rinke, P.; Blum, V.; Wieferink, J.; Tkatchenko, A.; Sanfilippo, A.; Reuter, K.; Scheffler, M. Resolution-of-identity approach to Hartree-Fock, hybrid density functionals, RPA, MP2 and GW with numeric atom-centered orbital basis functions. *New J. Phys.* **2012**, *14*, 053020.

(135) Van Setten, M. J.; Weigend, F.; Evers, F. The GW-method for quantum chemistry applications: Theory and implementation. *J. Chem. Theory Comput.* **2013**, *9*, 232–246.

(136) Caruso, F.; Rinke, P.; Ren, X.; Rubio, A.; Scheffler, M. Self-consistent GW: All-electron implementation with localized basis functions. *Phys. Rev. B* **2013**, *88*, 1–18.

(137) Kaplan, F.; Harding, M. E.; Seiler, C.; Weigend, F.; Evers, F.; Van Setten, M. J. Quasi-Particle Self-Consistent GW for Molecules. *J. Chem. Theory Comput.* **2016**, *12*, 2528–2541.

(138) Krause, K.; Klopper, W. Implementation of the Bethe-Salpeter equation in the TUR-BOMOLE program. *J. Comput. Chem.* **2017**, *38*, 383–388.

(139) Tirimbò, G.; Sundaram, V.; Çaylak, O.; Scharpach, W.; Sijen, J.; Junghans, C.; Brown, J.; Ruiz, F. Z.; Renaud, N.; Wehner, J.; Baumeier, B. Excited-state electronic structure of molecules using many-body Green’s functions: Quasiparticles and electron-hole excitations with VOTCA-XTP. *J. Chem. Phys.* **2020**, *152*, 114103.

(140) Watson, M. A.; Handy, N. C.; Cohen, A. J. Density functional calculations, using Slater basis sets, with exact exchange. *J. Chem. Phys.* **2003**, *119*, 6475–6481.

(141) Polly, R.; Werner, H. J.; Manby, F. R.; Knowles, P. J. Fast Hartree-Fock theory using local density fitting approximations. *Mol. Phys.* **2004**, *102*, 2311–2321.

(142) Sodt, A.; Subotnik, J. E.; Head-Gordon, M. Linear scaling density fitting. *J. Chem. Phys.* **2006**, *125*, 194109.

(143) Sodt, A.; Head-Gordon, M. Hartree-Fock exchange computed using the atomic resolution of the identity approximation. *J. Chem. Phys.* **2008**, *128*.

(144) Almlöf, J. Elimination of energy denominators in Møller-Plesset perturbation theory by a Laplace transform approach. *Chem. Phys. Lett.* **1991**, *181*, 319–320.

(145) Häser, M.; Almlöf, J. Laplace transform techniques in Møller-Plesset perturbation theory. *J. Chem. Phys.* **1992**, *96*, 489–494.

(146) Häser, M. Møller-Plesset (MP2) perturbation theory for large molecules. *Theor. Chim. Acta* **1993**, *87*, 147–173.

(147) H. N. Rojas,; R.W.Godby,; R. J. Needs, Space-Time Method for Ab Initio Calculations of Self-Energies and Dielectric Response Functions of Solids. *Phys. Rev. Lett.* **1995**, *74*, 1827–1831.

(148) Rieger, M. M.; Steinbeck, L.; White, I. D.; Rojas, H. N.; Godby, R. W. GW space-time method for the self-energy of large systems. *Comput. Phys. Commun.* **1999**, *117*, 211–228.

(149) Guerra, C. F.; Snijders, J. G.; te Velde, G.; Baerends, E. J. Towards an order-N DFT method. *Theor. Chem. Acc.* **1998**, *99*, 391–403.

(150) Krykunov, M.; Ziegler, T.; Van Lenthe, E. Hybrid density functional calculations of nuclear magnetic shieldings using slater-type orbitals and the zeroth- order regular approximation. *Int. J. Quantum Chem.* **2009**, *109*, 1676–1683.

(151) Merlot, P.; Kjærgaard, T.; Helgaker, T.; Lindh, R.; Aquilante, F.; Reine, S.; Pedersen, T. B. Attractive electron-electron interactions within robust local fitting approximations. *J. Comput. Chem.* **2013**, *34*, 1486–1496.

(152) Hollman, D. S.; Schaefer, H. F.; Valeev, E. F. Semi-exact concentric atomic density fitting: Reduced cost and increased accuracy compared to standard density fitting. *J. Chem. Phys.* **2014**, *140*, 064109.

(153) Mejía-Rodríguez, D.; Köster, A. M. Robust and efficient variational fitting of Fock exchange. *J. Chem. Phys.* **2014**, *141*, 124114.

(154) Manzer, S. F.; Epifanovsky, E.; Head-Gordon, M. Efficient implementation of the pair atomic resolution of the identity approximation for exact exchange for hybrid and range-separated density functionals. *J. Chem. Theory Comput.* **2015**, *11*, 518–527.

(155) Lewis, C. A.; Calvin, J. A.; Valeev, E. F. Clustered Low-Rank Tensor Format: Introduction and Application to Fast Construction of Hartree-Fock Exchange. *J. Chem. Theory Comput.* **2016**, *12*, 5868–5880.

(156) Hollman, D. S.; Schaefer, H. F.; Valeev, E. F. Fast construction of the exchange operator in an atom-centred basis with concentric atomic density fitting. *Mol. Phys.* **2017**, *115*, 2065–2076.

(157) Lin, P.; Ren, X.; He, L. Hybrid Functional Calculations with Numerical Atomic Orbitals On the Accuracy of Localized Resolution-of-the-Identity in Periodic Hybrid Functional Calculations with Numerical Atomic Orbitals. *J. Phys. Chem. Lett.* **2020**, *11*, 3082–3088.

(158) Rebolini, E.; Izsák, R.; Reine, S. S.; Helgaker, T.; Pedersen, T. B. Comparison of Three Efficient Approximate Exact-Exchange Algorithms: The Chain-of-Spheres Algorithm, Pair-Atomic Resolution-of-the-Identity Method, and Auxiliary Density Matrix Method. *J. Chem. Theory Comput.* **2016**, *12*, 3514–3522.

(159) Wirz, L. N.; Reine, S. S.; Pedersen, T. B. On Resolution-of-the-Identity Electron Repulsion Integral Approximations and Variational Stability. *J. Chem. Theory Comput.* **2017**, *13*, 4897–4906.

(160) Ihrig, A. C.; Wieferink, J.; Zhang, I. Y.; Ropo, M.; Ren, X.; Rinke, P.; Scheffler, M.; Blum, V. Accurate localized resolution of identity approach for linear-scaling hybrid density functionals and for many-body perturbation theory. *New J. Phys.* **2015**, *17*, 093020.

(161) Tew, D. P. Communication: Quasi-robust local density fitting. *J. Chem. Phys.* **2018**, *148*, 011102.

(162) Förster, A.; Franchini, M.; van Lenthe, E.; Visscher, L. A Quadratic Pair Atomic

Resolution of the Identity Based SOS-AO-MP2 Algorithm Using Slater Type Orbitals.

J. Chem. Theory Comput. **2020**, *16*, 875–891.

(163) Förster, A.; Visscher, L. Double hybrid DFT calculations with Slater type orbitals. *J. Comput. Chem.* **2020**, *41*, 1660–1684.

(164) Kaltak, M.; Klimeš, J.; Kresse, G. Low scaling algorithms for the random phase approximation: Imaginary time and laplace transformations. *J. Chem. Theory Comput.* **2014**, *10*, 2498–2507.

(165) Kaltak, M.; Klimeš, J.; Kresse, G. Cubic scaling algorithm for the random phase approximation: Self-interstitials and vacancies in Si. *Phys. Rev. B* **2014**, *90*, 1–11.

(166) Liu, P.; Kaltak, M.; Klimeš, J.; Kresse, G. Cubic scaling GW: Towards fast quasiparticle calculations. *Phys. Rev. B* **2016**, *94*, 1–13.

(167) Grumet, M.; Liu, P.; Kaltak, M.; Klimeš, J.; Kresse, G. Beyond the quasiparticle approximation: Fully self-consistent GW calculations. *Phys. Rev. B* **2018**, *98*, 1–9.

(168) Wilhelm, J.; Seewald, P.; Del Ben, M.; Hutter, J. Large-Scale Cubic-Scaling Random Phase Approximation Correlation Energy Calculations Using a Gaussian Basis. *J. Chem. Theory Comput.* **2016**, *12*, 5851–5859.

(169) Duchemin, I.; Blase, X. Separable resolution-of-the-identity with all-electron Gaussian bases: Application to cubic-scaling RPA. *J. Chem. Phys.* **2019**, *150*, 174120.

(170) Van Schilfgaarde, M.; Kotani, T.; Faleev, S. Quasiparticle self-consistent GW theory. *Phys. Rev. Lett.* **2006**, *96*, 1–4.

(171) Kotani, T.; Van Schilfgaarde, M.; Faleev, S. V. Quasiparticle self-consistent GW method: A basis for the independent-particle approximation. *Phys. Rev. B - Condens. Matter Mater. Phys.* **2007**, *76*, 1–24.

(172) te Velde, G.; Bickelhaupt, F. M.; Baerends, E. J.; Fonseca Guerra, C.; van Gisbergen, S.; Snijders, J. G.; Ziegler, T. Chemistry with ADF. *J. Comput. Chem.* **2001**, *22*, 931–967.

(173) Baerends, E.; Ziegler, T.; Atkins, A.; Autschbach, J.; Baseggio, O.; Bashford, D.; Bérçes, A.; Bickelhaupt, F.; Bo, C.; Boerrigter, P.; Cavallo, L.; Daul, C.; Chong, D.; Chulhai, D.; Deng, L.; Dickson, R.; Dieterich, J.; Ellis, D.; van Faassen, M.; Fan, L.; Fischer, T.; Förster, A.; Guerra, C. F.; Franchini, M.; Ghysels, A.; Giammona, A.; van Gisbergen, S.; Goez, A.; Götz, A.; Groeneveld, J.; Gritsenko, O.; Grüning, M.; Gusarov, S.; Harris, F.; van den Hoek, P.; Hu, Z.; Jacob, C.; Jacobsen, H.; Jensen, L.; Joubert, L.; Kaminski, J.; van Kessel, G.; König, C.; Kootstra, F.; Kovalenko, A.; Krykunov, M.; van Lenthe, E.; McCormack, D.; Michalak, A.; Mitoraj, M.; Morton, S.; Neugebauer, J.; Nicu, V.; Noddleman, L.; Osinga, V.; Patchkovskii, S.; Pavanello, M.; Peeples, C.; Philipsen, P.; Post, D.; Pye, C.; Ramanantoanina, H.; Ramos, P.; Ravenek, W.; Rodríguez, J.; Ros, P.; Rüger, R.; Schipper, P.; Schlüns, D.; van Shoot, H.; Schreckenbach, G.; Seldenthuis, J.; Seth, M.; Snijders, J.; Solà, M.; Stener, M.; Swart, M.; Swerhone, D.; Tognetti, V.; te Velde, G.; Vernooijs, P.; Ver-sluis, L.; Visscher, L.; Visser, O.; Wang, F.; Wesolowski, T.; van Wezenbeek, E.; Wiesenekker, G.; Wolff, S.; Woo, T.; Yakovlev, A. ADF2019.3, SCM, Theoretical Chemistry, Vrije Universiteit, Amsterdam, The Netherlands, <https://www.scm.com>.

(174) Stan, A.; Dahlen, N. E.; Van Leeuwen, R. Levels of self-consistency in the GW approximation. *J. Chem. Phys.* **2009**, *130*, 114105.

(175) Cancés, E.; Gontier, D.; Stoltz, G. A mathematical analysis of the GW0 method for computing electronic excited energies of molecules. *Rev. Math. Phys.* **2016**, *28*, 1650008.

(176) Han, X. J.; Liao, H. J.; Xie, H. D.; Huang, R. Z.; Meng, Z. Y.; Xiang, T. Analytic Continuation with Padé Decomposition. *Chinese Phys. Lett.* **2017**, *34*, 1–4.

(177) Surján, P. R. The MP2 energy as a functional of the Hartree-Fock density matrix. *Chem. Phys. Lett.* **2005**, *406*, 318–320.

(178) Starke, R.; Kresse, G. Self-consistent Green function equations and the hierarchy of approximations for the four-point propagator. *Phys. Rev. B* **2012**, *85*, 1–9.

(179) Schutski, R.; Zhao, J.; Henderson, T. M.; Scuseria, G. E. Tensor-structured coupled cluster theory. *J. Chem. Phys.* **2017**, *147*, 184113.

(180) Kohn, W. Density functional and density matrix method scaling linearly with the number of atoms. *Phys. Rev. Lett.* **1996**, *76*, 3168–3171.

(181) Baer, R.; Head-Gordon, M. Sparsity of the density matrix in kohn-sham density functional theory and an assessment of linear system-size scaling methods. *Phys. Rev. Lett.* **1997**, *79*, 3962–3965.

(182) Goedecker, S. Linear scaling electronic structure methods. *Rev. Mod. Phys.* **1999**, *71*, 1085–1123.

(183) Schindlmayr, A. Decay properties of the one-particle Green function in real space and imaginary time. *Phys. Rev. B* **2000**, *62*, 12573–12576.

(184) Zienau, J.; Clin, L.; Doser, B.; Ochsenfeld, C. Cholesky-decomposed densities in laplace-based second-order möller-plesset perturbation theory. *J. Chem. Phys.* **2009**, *130*, 204112.

(185) Maurer, S. A.; Kussmann, J.; Ochsenfeld, C. Communication: A reduced scaling J-engine based reformulation of SOS-MP2 using graphics processing units. *J. Chem. Phys.* **2014**, *141*, 051106.

(186) Maurer, S. A.; Clin, L.; Ochsenfeld, C. Cholesky-decomposed density MP2 with density fitting: Accurate MP2 and double-hybrid DFT energies for large systems. *J. Chem. Phys.* **2014**, *140*, 224112.

(187) Schurkus, H. F.; Ochsenfeld, C. Communication: An effective linear-scaling atomic-orbital reformulation of the random-phase approximation using a contracted double-Laplace transformation. *J. Chem. Phys.* **2016**, *144*, 031101.

(188) Luenser, A.; Schurkus, H. F.; Ochsenfeld, C. Vanishing-Overhead Linear-Scaling Random Phase Approximation by Cholesky Decomposition and an Attenuated Coulomb-Metric. *J. Chem. Theory Comput.* **2017**, *13*, 1647–1655.

(189) Graf, D.; Beuerle, M.; Schurkus, H. F.; Luenser, A.; Savasci, G.; Ochsenfeld, C. Accurate and Efficient Parallel Implementation of an Effective Linear-Scaling Direct Random Phase Approximation Method. *J. Chem. Theory Comput.* **2018**, *14*, 2505–2515.

(190) Graf, D.; Beuerle, M.; Ochsenfeld, C. Low-Scaling Self-Consistent Minimization of a Density Matrix Based Random Phase Approximation Method in the Atomic Orbital Space. *J. Chem. Theory Comput.* **2019**, *15*, 4468–4477.

(191) Rudberg, E.; Rubensson, E. H.; Sałek, P. Hartree-Fock calculations with linearly scaling memory usage. *J. Chem. Phys.* **2008**, *128*, 184106.

(192) Rudberg, E.; Rubensson, E. H.; Sałek, P. Kohn-sham density functional theory electronic structure calculations with linearly scaling computational time and memory usage. *J. Chem. Theory Comput.* **2011**, *7*, 340–350.

(193) Vandevondele, J.; Borštník, U.; Hutter, J. Linear scaling self-consistent field calculations with millions of atoms in the condensed phase. *J. Chem. Theory Comput.* **2012**, *8*, 3565–3573.

(194) Eichkorn, K.; Treutler, O.; Öhm, H.; Häser, M.; Ahlrichs, R. Auxiliary basis sets to approximate Coulomb potentials. *Chem. Phys. Lett.* **1995**, *240*, 283–290.

(195) Klahn, B.; Bingel, W. A. Completeness and Linear Independence of Basis Sets Used in Quantum Chemistry. *Int. J. Quantum Chem.* **1977**, *XI*, 943–957.

(196) Löwdin, P. O. Group algebra, convolution algebra, and applications to quantum mechanics. *Rev. Mod. Phys.* **1967**, *39*, 259–287.

(197) Kudin, K. N.; Scuseria, G. E. Linear-scaling density-functional theory with Gaussian orbitals and periodic boundary conditions: Efficient evaluation of energy and forces via the fast multipole method. *Phys. Rev. B* **2000**, *61*, 16440–16453.

(198) Suhai, S.; Bagus, P. S.; Ladik, J. An error analysis for Hartree-Fock crystal orbital calculations. *Chem. Phys.* **1982**, *68*, 467–471.

(199) Kudin, K. N.; Scuseria, G. E.; Cancès, E. A black-box self-consistent field convergence algorithm: One step closer. *J. Chem. Phys.* **2002**, *116*, 8255–8261.

(200) Lehtola, S.; Blockhuys, F.; Van Alsenoy, C. An overview of self-consistent field calculations within finite basis sets. *Molecules* **2020**, *25*, 1–23.

(201) Schipper, P. R.; Gritsenko, O. V.; Van Gisbergen, S. J.; Baerends, E. J. Molecular calculations of excitation energies and (hyper)polarizabilities with a statistical average of orbital model exchange-correlation potentials. *J. Chem. Phys.* **2000**, *112*, 1344–1352.

(202) De Jong, G. T.; Visscher, L. Using the locality of the small-component density in molecular Dirac-Hartree-Fock calculations. *Theor. Chem. Acc.* **2002**, *107*, 304–308.

(203) Takatsuka, A.; Ten-no, S.; Hackbusch, W. Minimax approximation for the decomposition of energy denominators in Laplace-transformed MøllerPlesset perturbation theories. *J. Chem. Phys.* **2008**, *129*, 044112.

(204) Helmich-Paris, B.; Visscher, L. Improvements on the minimax algorithm for the Laplace transformation of orbital energy denominators. *J. Comput. Phys.* **2016**, *321*, 927–931.

(205) Levenberg, K. A method for the solution of certain non-linear problems in least squares. *Q. Appl. Math.* **1944**, *2*, 164–168.

(206) Marquardt, D. W. An algorithm for least-squares estimation of nonlinear parameters. *J. Soc. Ind. Appl. Math.* **1963**, *11*, 431–441.

(207) Source code available on <https://github.com/bhelmichparis/laplace-minimax>.

(208) Vidberg, H. J.; Serene, J. W. Solving the Eliashberg equations by means of N-point Padé approximants. *J. Low Temp. Phys.* **1977**, *29*, 179–192.

(209) Wilhelm, J.; Del Ben, M.; Hutter, J. GW in the Gaussian and Plane Waves Scheme with Application to Linear Acenes. *J. Chem. Theory Comput.* **2016**, *12*, 3623–3635.

(210) Govoni, M.; Galli, G. GW100: Comparison of Methods and Accuracy of Results Obtained with the WEST Code. *J. Chem. Theory Comput.* **2018**, *14*, 1895–1909.

(211) Franchini, M.; Philipsen, P. H. T.; Van Lenthe, E.; Visscher, L. Accurate Coulomb potentials for periodic and molecular systems through density fitting. *J. Chem. Theory Comput.* **2014**, *10*, 1994–2004.

(212) Ernzerhof, M.; Scuseria, G. E. Assessment of the PerdewBurkeErnzerhof exchange-correlation functional. *J. Chem. Phys.* **1999**, *110*, 5029.

(213) Adamo, C.; Barone, V. Toward reliable density functional methods without adjustable parameters: The PBE0 model. *J. Chem. Phys.* **1999**, *110*, 6158–6170.

(214) Stuke, A.; Kunkel, C.; Golze, D.; Todorović, M.; Margraf, J. T.; Reuter, K.; Rinke, P.; Oberhofer, H. Atomic structures and orbital energies of 61,489 crystal-forming organic molecules. *Sci. Data* **2020**, *7*, 1–11.

(215) Data donwloaded from the website of the GW100 project by Van Setten et al., <https://gw100.wordpress.com> (accessed on 2020-06-10).

(216) Chong, D. P.; Van Lenthe, E.; Van Gisbergen, S.; Baerends, E. J. Even-tempered slater-type orbitals revisited: From hydrogen to krypton. *J. Comput. Chem.* **2004**, *25*, 1030–1036.

(217) Van Lenthe, E.; Baerends, J. E. Optimized Slatertype basis sets for the elements 1118. *J. Comput. Chem.* **2003**, *24*, 1142–1156.

(218) Details of the composition of the fit sets can be found in the supporting information of our recent work.¹⁶²

(219) The individual numbers of points can differ. This is due to the fact that we adjust the grid sizes at runtime to match a certain error parameter. Thus, for many systems, the number of points will actually be smaller than 18, since the imaginary time and frequency integrals are already converged with a smaller number of points.

(220) Van Lenthe, E.; Baerends, E. J.; Snijders, J. G. Relativistic regular two-component hamiltonians. *J. Chem. Phys.* **1993**, *99*, 4597.

(221) Van Lenthe, E.; Baerends, E. J.; Snijders, J. G. Relativistic total energy using regular approximations. *J. Chem. Phys.* **1994**, *101*, 9783–9792.

(222) Van Lenthe, E.; Snijders, J. G.; Baerends, E. J. The zero-order regular approximation for relativistic effects: The effect of spin-orbit coupling in closed shell molecules. *J. Chem. Phys.* **1996**, *105*, 6505–6516.

(223) Van Lenthe, E.; Ehlers, A.; Baerends, J. E. Geometry optimizations in the zero order regular approximation for relativistic effects. *J. Chem. Phys.* **1999**, *110*, 8943–8953.

(224) Payne, M. C.; Teter, M. P.; Allan, D. C.; Arias, T. A.; Joannopoulos, J. D. Iterative minimization techniques for ab initio total-energy molecular dynamics and conjugate gradients calculations :. *Rev. Mod. Phys.* **1992**, *64*, 1045–1097.

(225) Varga, K.; Zhang, Z.; Pantelides, S. T. "Lagrange functions": A family of powerful basis sets for real-space order-N electronic structure calculations. *Phys. Rev. Lett.* **2004**, *93*, 1–4.

(226) Maggio, E.; Liu, P.; Van Setten, M. J.; Kresse, G. GW100: A Plane Wave Perspective for Small Molecules. *J. Chem. Theory Comput.* **2017**, *13*, 635–648.

(227) Gao, W.; Chelikowsky, J. R. Real-Space Based Benchmark of G0W0 Calculations on GW100: Effects of Semicore Orbitals and Orbital Reordering. *J. Chem. Theory Comput.* **2019**, *15*, 5299–5307.

(228) These reference values have been calculated by Chelikowsky and coworkers with the nanoGW²²⁹ package which implements *GW* in RS and with a full frequency treatment. The calculations have been performed using KS orbitals and energies calculated with the PARSEC code.²²⁷ For details we refer to the original work²²⁷.

(229) Tiago, M. L.; Chelikowsky, J. R. Optical excitations in organic molecules, clusters, and defects studied by first-principles Green's function methods. *Phys. Rev. B* **2006**, *73*, 1–19.

(230) Balasubramani, S. G.; Chen, G. P.; Coriani, S.; Diedenhofen, M.; Frank, M. S.; Franzke, Y. J.; Furche, F.; Grotjahn, R.; Harding, M. E.; Hättig, C.; Hellweg, A.; Helmich-Paris, B.; Holzer, C.; Huniar, U.; Kaupp, M.; Khah, A. M.; Khani, S. K.; Müller, T.; Mack, F.; Nguyen, B. D.; Parker, S. M.; Perlt, E.; Rappoport, D.; Reiter, K.; Roy, S.; Rückert, M.; Schmitz, G.; Sierka, M.; Tapavicza, E.; Tew, D. P.; van Wüllen, C.; Voora, V. K.; Weigend, F.; Wodyniski, A.; Yu, J. M. TURBOMOLE : Modular program suite for ab initio quantum-chemical and condensed-matter simulations. *J. Chem. Phys.* **2020**, 184107.

(231) Pritchard, B. P.; Altarawy, D.; Didier, B.; Gibson, T. D.; Windus, T. L. New Basis Set

Exchange: An Open, Up-to-Date Resource for the Molecular Sciences Community. *J. Chem. Inf. Model.* **2019**, *59*, 4814–4820.

(232) Boulanger, P.; Jacquemin, D.; Duchemin, I.; Blase, X. Fast and accurate electronic excitations in cyanines with the many-body bethe-salpeter approach. *J. Chem. Theory Comput.* **2014**, *10*, 1212–1218.

(233) Faber, C.; Boulanger, P.; Attaccalite, C.; Cannuccia, E.; Duchemin, I.; Deutsch, T.; Blase, X. Exploring approximations to the GW self-energy ionic gradients. *Phys. Rev. B* **2015**, *91*, 1–10.

(234) Jacquemin, D.; Duchemin, I.; Blase, X. Benchmarking the Bethe-Salpeter Formalism on a Standard Organic Molecular Set. *J. Chem. Theory Comput.* **2015**, *11*, 3290–3304.

(235) Bruneval, F.; Hamed, S. M.; Neaton, J. B. A systematic benchmark of the ab initio Bethe-Salpeter equation approach for low-lying optical excitations of small organic molecules. *J. Chem. Phys.* **2015**, *142*, 244101.

(236) The structures of the water clusters have been downloaded from the website of the ERGO program,⁷ <http://www.ergoscf.org> (visited on may 19th, 2020).

(237) Lange, M. F.; Berkelbach, T. C. On the Relation between Equation-of-Motion Coupled-Cluster Theory and the GW Approximation. *J. Chem. Theory Comput.* **2018**, *14*, 4224–4236.

(238) Weigend, F.; Häser, M.; Patzelt, H.; Ahlrichs, R. RI-MP2: Optimized auxiliary basis sets and demonstration of efficiency. *Chem. Phys. Lett.* **1998**, *294*, 143–152.

(239) Hättig, C.; Weigend, F. CC2 excitation energy calculations on large molecules using the resolution of the identity approximation. *J. Chem. Phys.* **2000**, *113*, 5154–5161.

(240) Weigend, F.; Köhn, A.; Hättig, C. Efficient use of the correlation consistent basis sets in resolution of the identity MP2 calculations. *J. Chem. Phys.* **2002**, *116*, 3175–3183.

(241) Werner, H. J.; Manby, F. R.; Knowles, P. J. Fast linear scaling second-order Møller-Plesset perturbation theory (MP2) using local and density fitting approximations. *J. Chem. Phys.* **2003**, *118*, 8149–8160.

(242) Schütz, M.; Manby, F. R. Linear scaling local coupled cluster theory with density fitting. Part I: 4-external integrals. *Phys. Chem. Chem. Phys.* **2003**, *5*, 3349–3358.

(243) Hättig, C. Geometry optimizations with the coupled-cluster model CC2 using the resolution-of-the-identity approximation. *J. Chem. Phys.* **2003**, *118*, 7751–7761.

(244) Klopper, W.; Manby, F. R.; Ten-No, S.; Valeev, E. F. R12 methods in explicitly correlated molecular electronic structure theory. *Int. Rev. Phys. Chem.* **2006**, *25*, 427–468.

Supporting Information for: Low-order scaling

G_0W_0 by pair atomic density fitting

Arno Förster* and Lucas Visscher

*Theoretical Chemistry, Vrije Universiteit, De Boelelaan 1083, NL-1081 HV, Amsterdam,
The Netherlands*

E-mail: a.t.l.foerster@vu.nl

Contents

List of Figures	S1
List of Tables	S1
S1 Additional figures	S2
S2 Thresholds	S2
S3 GW100 QP Energies	S4
S4 GW5000 QP Energies	S10
S5 Numerical frequency integration	S16
References	S17

List of Figures

S1	Errors for the HOMO-LUMO QP gap on the G_0W_0 @PBE level of theory . . .	S2
----	--	----

List of Tables

S1	Thresholds controlling distance effects in the PADF- G_0W_0 algorithm. All values are in Bohr.	S3
S2	G_0W_0 @PBE HOMO QP energies for the GW100 database	S4
S3	G_0W_0 @PBE LUMO QP energies for the GW100 database	S6
S4	G_0W_0 @PBE0 HOMO and LUMO QP energies for the GW100 database . . .	S8
S5	G_0W_0 @PBE0 HOMO QP energies for 20 large systems from GW5000 . . .	S10
S6	G_0W_0 @PBE0 LUMO QP energies for 20 large systems from GW5000 . . .	S11
S7	G_0W_0 @PBE0 HOMO and LUMO QP energies for 250 randomly selected systems from GW5000	S12
S8	Parameters of the linear fits $f(x) = a \times x + b$	S16

S1 Additional figures

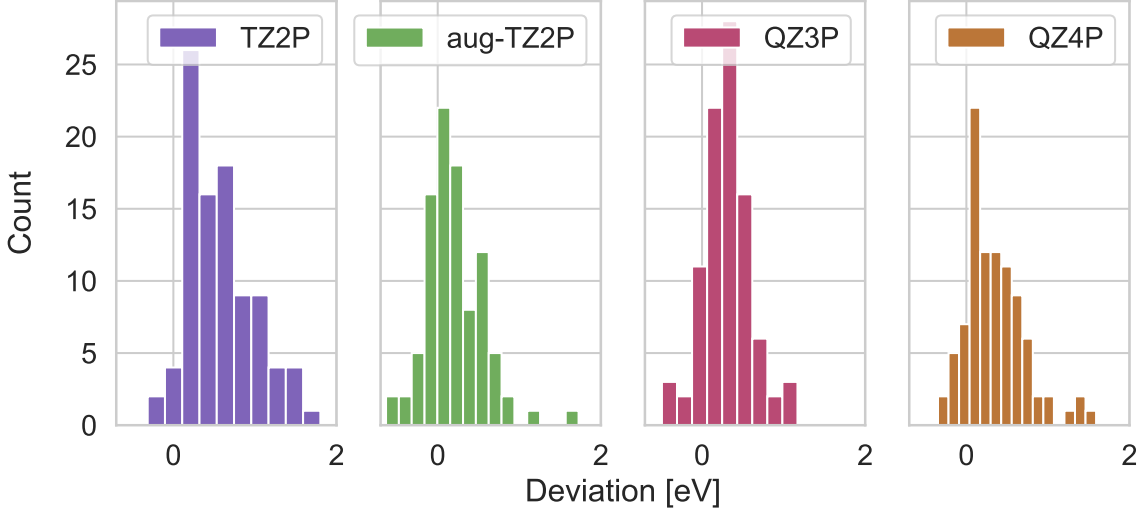


Figure S1: Distribution of errors for the HOMO-LUMO QP gap on the G_0W_0 @PBE level of theory using four different STO-type basis sets. The error is in eV and with respect to the reference by Chelikowsky and coworkers.¹

S2 Thresholds

Beside from PADF, we employ further local approximations to reduce the asymptotic scaling of our algorithm from cubic to quadratic. For more details we refer to our recent work describing our MP2 implementation.²

A basis function is considered negligible for $|\mathbf{r}| > d_\mu$ if

$$|\chi_\mu(\mathbf{r})| < \epsilon_{bas} \quad \forall |\mathbf{r}| > d_\mu , \quad (1)$$

which implies that $C_{\mu\nu\beta}^{ABB} = C_{\nu\mu\alpha}^{BAA} = 0$ whenever

$$|\mathbf{R}_A - \mathbf{R}_B| > d_\mu + d_\nu , \quad (2)$$

and ϵ_{bas} is some (small) positive real number. In the same way, the interaction between two pair densities $\chi_\mu\chi_\nu$, $\chi_\kappa\chi_\lambda$ is evaluated via multipole expansion³ (recall, that the fit functions

are always assumed to be centered on the second atom of the pair) if

$$|\mathbf{R}_B - \mathbf{R}_D| < d_\beta + d_\delta \quad \forall \beta, \delta , \quad (3)$$

where d is defined by

$$|f_\beta(\mathbf{r})| < \epsilon_{multi} \quad \forall |\mathbf{r}| > d_\beta . \quad (4)$$

This is graphically illustrated in figure 1 in reference 2 (where we denoted ϵ_{bas} by ϑ_{DCAB} , the procedure for ϵ_{multi} is the same).

Finally, when the Coulomb potential due to atom A , $V_c^A(\mathbf{r})$, does not overlap with any basis function on atom B , i.e. whenever

$$|\mathbf{R}_A - \mathbf{R}_B| < d_C + d_\nu \quad \forall \nu \in B , \quad (5)$$

where d_C denotes the distance for which

$$|V_c^A(\mathbf{r})| < \epsilon_C \quad \forall |\mathbf{r}| > d_C , \quad (6)$$

the two atoms are defined as non-interacting. The values for the three thresholds we used in this work for all GW -calculations are given in S1.

Table S1: Thresholds controlling distance effects in the PADF- G_0W_0 algorithm. All values are in Bohr.

	<i>Basic</i>	<i>Normal</i>	<i>Good</i>
ϵ_{multi}	1×10^{-2}	5×10^{-3}	1×10^{-3}
ϵ_{bas}	1×10^{-3}	3×10^{-4}	1×10^{-4}
ϵ_C	3×10^{-2}	1×10^{-2}	1×10^{-3}

S3 GW100 QP Energies

All values are also available in .CVS format

Table S2: G_0W_0 @PBE HOMO QP energies for the GW100 database (all values in eV).

	Name	TZ2P	aug-TZ2P	QZ3P	QZ4P
1	Helium	-22.904	-22.716	-23.102	-23.063
2	Neon	-20.087	-20.048	-20.077	-19.821
3	Argon	-14.707	-14.585	-14.698	-14.663
4	Krypton	-13.113	-12.990	-13.171	-13.483
5	Xenon	-11.546	-11.543	-11.690	-11.690
6	Hydrogen	-15.490	-15.731	-15.812	-15.732
7	Lithium dimer	-4.763	-4.839	-4.814	-4.921
8	Sodium dimer	-4.634	-4.676	-4.769	-4.783
9	Sodium tetramer	-3.905	-3.970	-4.039	-4.006
10	Sodium hexamer	-3.992	-4.057	-4.160	-4.149
11	Potassium dimer	-3.795	-3.812	-3.807	-4.029
12	Rubidium dimer	-3.669	-3.710	-3.959	-3.959
13	Nitrogen	-14.521	-14.293	-14.536	-14.682
14	Phosphorus dimer	-9.785	-9.783	-9.877	-9.818
15	Arsenic dimer	-9.057	-9.050	-9.195	-9.489
16	Fluorine	-14.389	-14.279	-14.606	-14.572
17	Chlorine	-10.714	-10.675	-10.816	-10.600
18	Bromine	-9.882	-9.769	-9.811	-10.089
19	Iodine	-9.188	-8.808	-8.704	-8.701
20	Methane	-13.663	-13.675	-13.796	-13.805
21	Ethane	-12.146	-12.161	-12.237	-12.285
22	Propane	-11.576	-11.608	-11.672	-11.696
23	Butane	-11.279	-11.319	-11.368	-11.398
24	Ethylene	-10.034	-10.013	-10.232	-10.190
25	Acetylene	-10.733	-10.774	-10.790	-10.882
26	Tetracarbon	-10.352	-10.500	-10.591	-10.633
27	Cyclopropane	-10.312	-10.301	-10.392	-10.401
28	Benzene	-8.638	-8.557	-8.844	-8.945
29	Cyclooctatetraene	-7.792	-7.836	-7.890	-8.016
30	Cyclopentadiene	-8.089	-8.042	-8.193	-8.312
31	Vinyl fluoride	-9.715	-9.899	-9.957	-10.058
32	Vinyl chloride	-9.429	-9.467	-9.535	-9.518
33	Vinyl bromide	-9.158	-9.098	-9.349	-9.238
34	Vinyl iodide	-8.777	-8.731	-8.806	-8.819
35	Tetrafluoromethane	-14.731	-14.573	-14.946	-14.989
36	Tetrachloromethane	-10.639	-10.558	-10.681	-10.706
37	Tetrabromomethane	-9.592	-9.722	-9.738	-9.971
38	Tetraiodomethane	-8.604	-8.462	-8.649	-8.666
39	Silane	-12.071	-12.101	-12.222	-12.164
40	Germane	-11.796	-11.864	-11.853	-11.975
41	Disilane	-10.027	-10.435	-10.145	-10.166
42	Pentasilane	-8.730	-8.708	-8.750	-8.821
43	Lithium hydride	-6.984	-6.767	-6.846	-6.980
44	Potassium hydride	-4.641	-4.658	-5.175	-5.530
45	Borane	-12.654	-12.682	-12.753	-12.766
46	Diborane(6)	-11.643	-11.653	-11.720	-11.759
47	Amonia	-10.196	-9.889	-10.177	-10.100
48	Hydrazoic acid	-10.109	-10.053	-10.220	-10.234
49	Phosphine	-9.900	-9.813	-10.024	-10.045
50	Arsine	-9.821	-9.851	-9.917	-10.204

Continued on next page

	Name	TZ2P	aug-TZ2P	QZ3P	QZ4P
51	Hydrogen sulfide	-9.667	-9.652	-9.696	-9.839
52	Hydrogen fluoride	-14.883	-15.061	-15.023	-14.848
53	Hydrogen chloride	-11.925	-11.777	-11.957	-11.879
54	Lithium fluoride	-9.928	-9.603	-9.792	-9.932
55	Magnesium fluoride	-12.475	-12.005	-11.968	-12.191
56	Titanium tetrafluoride	-13.465	-13.475	-14.080	-13.450
57	Aluminum fluoride	-13.459	-13.845	-13.935	-13.936
58	Boron monofluoride	-10.269	-10.213	-10.247	-10.405
59	Sulfur tetrafluoride	-11.642	-11.678	-11.783	-11.808
60	Potassium bromide	-7.430	-7.405	-7.382	-7.848
61	Gallium monochloride	-9.295	-9.269	-9.324	-9.460
62	Sodium chloride	-8.664	-7.984	-8.118	-8.340
63	Magnesium chloride	-10.600	-10.660	-10.700	-10.767
64	Aluminum iodide	-9.056	-8.957	-9.061	-9.060
65	Boron nitride	-10.915	-10.859	-10.994	-10.808
66	Hydrogen cyanide	-12.920	-12.913	-13.023	-12.964
67	Phosphorus mononitride	-10.776	-11.316	-10.846	-10.873
68	Hydrazine	-9.182	-8.950	-9.133	-9.092
69	Formaldehyde	-9.974	-9.973	-10.129	-10.203
70	Methanol	-10.257	-10.140	-10.408	-10.371
71	Ethanol	-9.849	-9.784	-9.998	-9.991
72	Acetaldehyde	-9.159	-9.200	-9.398	-9.406
73	Ethoxy ethane	-8.949	-9.021	-9.136	-9.198
74	Formic acid	-10.318	-10.408	-10.440	-10.465
75	Hydrogen peroxide	-10.641	-10.494	-10.775	-10.862
76	Water	-11.774	-10.973	-11.815	-11.685
77	Carbon dioxide	-12.811	-12.820	-12.973	-12.927
78	Carbon disulfide	-9.344	-9.368	-9.456	-9.450
79	Carbon oxide sulfide	-10.529	-10.544	-10.614	-10.583
80	Carbon oxide selenide	-9.800	-9.809	-9.921	-10.230
81	Carbon monoxide	-13.328	-13.286	-13.308	-13.374
82	Ozone	-11.566	-11.372	-11.782	-11.677
83	Sulfur dioxide	-11.441	-11.472	-11.627	-11.580
84	Beryllium monoxide	-9.180	-9.120	-9.108	-9.356
85	Magnesium monoxide	-7.061	-6.651	-6.920	-6.933
86	Toluene	-8.285	-8.237	-8.466	-8.552
87	Ethylbenzene	-8.239	-8.183	-8.415	-8.435
88	Hexafluorobenzene	-9.192	-9.143	-9.277	-9.414
89	Phenol	-7.965	-7.984	-8.159	-8.150
90	Aniline	-7.425	-7.336	-7.497	-7.561
91	Pyridine	-8.774	-8.801	-9.064	-9.016
92	Guanine	-7.442	-7.429	-7.521	-7.618
93	Adenine	-7.640	-7.720	-7.783	-7.919
94	Cytosine	-7.952	-8.079	-8.071	-8.295
95	Thymine	-8.406	-8.434	-8.513	-8.616
96	Uracil	-8.746	-9.042	-9.140	-9.227
97	Urea	-8.716	-9.017	-9.006	-9.149
98	Silver dimer	-6.915	-6.940	-6.982	-6.972
99	Copper dimer	-7.621	-7.407	-7.356	-7.815
100	Copper cyanide	-9.812	-9.606	-9.563	-9.867

Table S3: G_0W_0 @PBE LUMO QP energies for the GW100 database (all values in eV).

	Name	TZ2P	aug-TZ2P	QZ3P	QZ4P
1	Helium	10.614	2.916	4.396	2.842
2	Neon	11.236	2.903	2.630	3.755
3	Argon	8.690	2.010	3.087	1.857
4	Krypton	7.593	1.648	1.386	1.433
5	Xenon	5.563	5.563	1.329	1.329
6	Hydrogen	3.389	2.035	2.229	2.797
7	Lithium dimer	-0.280	-0.316	-0.376	-0.357
8	Sodium dimer	-0.319	-0.343	-0.564	-0.413
9	Sodium tetramer	-0.546	-0.588	-0.722	-0.682
10	Sodium hexamer	-0.520	-0.733	-0.778	-0.689
11	Potassium dimer	-0.379	-0.365	-0.463	-0.526
12	Rubidium dimer	-0.477	-0.505	-0.663	-0.663
13	Nitrogen	3.134	2.786	2.758	2.681
14	Phosphorus dimer	-0.142	-0.290	-0.386	-0.406
15	Arsenic dimer	-0.442	-0.500	-0.528	-0.880
16	Fluorine	0.600	0.479	0.321	0.225
17	Chlorine	-0.133	-0.268	-0.359	-0.431
18	Bromine	-0.793	-0.866	-0.928	-1.060
19	Iodine	-1.090	-1.075	-1.346	-1.345
20	Methane	2.238	0.871	1.114	1.583
21	Ethane	2.169	0.859	1.084	1.480
22	Propane	2.095	0.789	1.011	1.421
23	Butane	2.082	0.704	0.970	1.373
24	Ethylene	2.470	2.194	2.360	2.084
25	Acetylene	3.317	2.871	3.195	2.912
26	Tetracarbon	-2.098	-2.206	-2.255	-2.332
27	Cyclopropane	2.327	0.847	1.131	1.557
28	Benzene	1.489	1.361	1.381	1.244
29	Cyclooctatetraene	0.514	0.412	0.352	0.220
30	Cyclopentadiene	1.454	1.313	1.329	1.198
31	Vinyl fluoride	2.601	2.304	2.474	2.204
32	Vinyl chloride	1.935	1.693	1.763	1.615
33	Vinyl bromide	1.757	1.552	1.623	1.588
34	Vinyl iodide	1.359	1.243	1.068	0.938
35	Tetrafluoromethane	2.362	1.363	0.988	2.584
36	Tetrachloromethane	0.650	0.457	0.373	0.322
37	Tetrabromomethane	-0.479	-0.574	-0.694	-0.672
38	Tetraiodomethane	-2.167	-1.680	-1.674	-1.691
39	Silane	1.856	0.945	1.084	1.148
40	Germane	1.669	1.000	1.185	1.160
41	Disilane	2.048	0.918	1.807	1.620
42	Pentasilane	0.601	0.262	0.338	0.168
43	Lithium hydride	0.102	0.036	0.033	0.018
44	Potassium hydride	0.037	-0.018	-0.067	-0.082
45	Borane	0.633	0.554	0.504	0.428
46	Diborane(6)	1.248	1.157	1.118	1.026
47	Amonia	1.933	0.907	1.105	1.044
48	Hydrazoic acid	2.051	1.791	1.778	1.678
49	Phosphine	1.604	0.841	0.951	1.237
50	Arsine	1.571	0.854	1.006	1.133
51	Hydrogen sulfide	1.701	0.955	1.017	1.014
52	Hydrogen fluoride	2.010	1.264	1.291	1.553
53	Hydrogen chloride	1.979	1.397	1.397	1.486
54	Lithium fluoride	0.131	0.088	0.100	0.079
55	Magnesium fluoride	0.089	0.001	-0.015	-0.064

Continued on next page

	Name	TZ2P	aug-TZ2P	QZ3P	QZ4P
56	Titanium tetrafluoride	0.961	0.941	0.887	0.595
57	Aluminum fluoride	0.636	0.318	0.265	0.068
58	Boron monofluoride	1.831	1.624	1.591	1.502
59	Sulfur tetrafluoride	1.121	0.879	0.795	0.458
60	Potassium bromide	-0.197	-0.208	-0.232	-0.229
61	Gallium monochloride	0.333	0.262	0.260	0.168
62	Sodium chloride	-0.228	-0.247	-0.257	-0.283
63	Magnesium chloride	-0.141	-0.184	-0.242	-0.304
64	Aluminum iodide	-0.345	-0.248	-0.402	-0.429
65	Boron nitride	-2.942	-3.006	-3.128	-3.172
66	Hydrogen cyanide	3.069	2.687	2.909	2.689
67	Phosphorus mononitride	0.481	0.259	0.188	0.137
68	Hydrazine	1.741	0.819	0.967	1.126
69	Formaldehyde	1.661	1.473	1.486	1.345
70	Methanol	2.090	1.025	1.188	1.446
71	Ethanol	1.981	0.936	1.097	1.380
72	Acetaldehyde	1.751	1.569	1.567	1.438
73	Ethoxy ethane	2.054	0.715	0.945	1.329
74	Formic acid	2.501	2.267	2.304	2.147
75	Hydrogen peroxide	2.962	2.558	2.613	2.390
76	Water	1.844	1.034	1.209	1.246
77	Carbon dioxide	4.169	1.286	1.629	1.114
78	Carbon disulfide	0.415	0.245	0.183	0.140
79	Carbon oxide sulfide	1.879	1.645	1.586	1.516
80	Carbon oxide selenide	1.495	1.360	1.299	1.283
81	Carbon monoxide	1.499	1.301	1.221	1.138
82	Ozone	-1.246	-1.445	-1.590	-1.671
83	Sulfur dioxide	-0.203	-0.409	-0.502	-0.575
84	Beryllium monoxide	-1.711	-1.777	-1.733	-1.878
85	Magnesium monoxide	-1.321	-1.435	-1.500	-1.539
86	Toluene	1.429	1.283	1.286	1.081
87	Ethylbenzene	1.467	1.311	1.309	1.121
88	Hexafluorobenzene	1.028	0.526	0.434	0.203
89	Phenol	1.429	1.280	1.293	1.161
90	Aniline	1.565	1.399	1.408	1.232
91	Pyridine	0.988	0.852	0.858	0.437
92	Guanine	1.196	0.992	0.913	0.801
93	Adenine	0.878	0.750	0.755	0.585
94	Cytosine	0.771	0.636	0.637	0.177
95	Thymine	0.602	0.460	0.438	-0.030
96	Uracil	0.562	0.431	0.414	0.034
97	Urea	1.443	0.620	0.745	0.901
98	Silver dimer	-0.669	-0.673	-0.762	-0.760
99	Copper dimer	-0.638	-0.657	-0.702	-0.961
100	Copper cyanide	-1.026	-1.088	-1.114	-1.181

Table S4: G_0W_0 @PBE0 LUMO QP energies for the GW100 database (all values in eV).

	Name	HOMO		LUMO	
		TZ2P	QZ4P	TZ2P	QZ4P
1	Helium	-23.202	-23.546	10.677	2.813
2	Neon	-20.402	-20.381	11.331	3.794
3	Argon	-14.989	-14.933	8.743	1.879
4	Krypton	-13.297	-13.474	7.653	1.447
5	Xenon	-11.761	-11.935	5.598	1.349
6	Hydrogen	-16.004	-16.099	3.282	2.658
7	Lithium dimer	-5.053	-5.182	-0.244	-0.314
8	Sodium dimer	-4.788	-4.931	-0.285	-0.378
9	Sodium tetramer	-4.058	-4.186	-0.515	-0.645
10	Sodium hexamer	-4.179	-4.348	-0.489	-0.666
11	Potassium dimer	-3.910	-4.105	-0.357	-0.496
12	Rubidium dimer	-3.808	-4.335	-0.384	-0.564
13	Nitrogen	-15.084	-15.071	3.093	2.661
14	Phosphorus dimer	-10.026	-10.095	-0.139	-0.381
15	Arsenic dimer	-9.238	-9.657	-0.440	-0.630
16	Fluorine	-14.899	-15.140	0.626	0.298
17	Chlorine	-10.995	-11.120	-0.083	-0.368
18	Bromine	-10.107	-10.290	-0.739	-1.002
19	Iodine	-9.131	-9.237	-1.103	-1.269
20	Methane	-14.044	-14.138	2.266	1.564
21	Ethane	-12.465	-12.574	2.216	1.476
22	Propane	-11.908	-12.012	2.163	1.430
23	Butane	-11.607	-11.724	2.162	1.387
24	Ethylene	-10.253	-10.325	2.532	2.208
25	Acetylene	-11.023	-11.112	3.408	2.977
26	Tetracarbon	-10.864	-11.014	-2.130	-2.347
27	Cyclopropane	-10.586	-10.694	2.373	1.537
28	Benzene	-8.933	-9.184	1.682	1.356
29	Cyclooctatetraene	-8.043	-8.223	0.666	0.430
30	Cyclopentadiene	-8.311	-8.454	1.606	1.345
31	Vinyl fluoride	-9.978	-10.281	2.675	2.337
32	Vinyl chloride	-9.709	-9.833	2.001	1.688
33	Vinyl bromide	-9.422	-9.752	1.820	1.543
34	Vinyl iodide	-8.831	-9.128	1.435	1.094
35	Tetrafluoromethane	-15.358	-15.642	2.354	2.596
36	Tetrachloromethane	-11.069	-11.163	0.711	0.391
37	Tetrabromomethane	-9.945	-10.151	-0.434	-0.657
38	Tetraiodomethane	-8.822	-8.938	-1.424	-1.640
39	Silane	-12.472	-12.592	1.876	1.315
40	Germane	-12.167	-12.290	1.663	1.037
41	Disilane	-10.343	-10.467	1.630	1.048
42	Pentasilane	-8.975	-9.120	0.769	0.334
43	Lithium hydride	-7.541	-7.521	0.016	-0.065
44	Potassium hydride	-5.721	-5.706	-0.016	-0.122
45	Borane	-13.034	-13.133	0.609	0.403
46	Diborane(6)	-12.024	-12.154	1.326	1.094
47	Amonia	-10.520	-10.486	1.923	1.309
48	Hydrazoic acid	-10.439	-10.573	2.006	1.625
49	Phosphine	-10.163	-10.321	1.609	1.223
50	Arsine	-10.022	-10.308	1.581	1.126
51	Hydrogen sulfide	-9.916	-10.012	1.671	1.128
52	Hydrogen fluoride	-15.260	-15.341	1.862	1.364
53	Hydrogen chloride	-12.137	-12.104	1.816	1.342
54	Lithium fluoride	-10.465	-10.517	-0.003	-0.033

Continued on next page

	Name	HOMO		LUMO	
		TZ2P	QZ4P	TZ2P	QZ4P
55	Magnesium fluoride	-13.498	-12.867	0.063	-0.064
56	Titanium tetrafluoride	-14.403	-14.498	0.357	0.025
57	Aluminum fluoride	-14.318	-14.613	0.675	0.297
58	Boron monofluoride	-10.663	-10.727	1.738	1.402
59	Sulfur tetrafluoride	-12.055	-12.278	1.124	0.734
60	Potassium bromide	-7.701	-7.738	-0.304	-0.355
61	Gallium monochloride	-9.472	-9.633	0.284	0.137
62	Sodium chloride	-8.495	-8.655	-0.337	-0.390
63	Magnesium chloride	-11.062	-11.265	-0.155	-0.311
64	Aluminum iodide	-9.300	-9.427	-0.200	-0.384
65	Boron nitride	-11.252	-11.387	-3.106	-3.269
66	Hydrogen cyanide	-13.248	-13.330	3.078	2.656
67	Phosphorus mononitride	-11.301	-11.458	0.452	0.127
68	Hydrazine	-9.459	-9.493	1.746	1.082
69	Formaldehyde	-10.399	-10.614	1.677	1.357
70	Methanol	-10.652	-10.790	2.066	1.356
71	Ethanol	-10.309	-10.434	1.995	1.326
72	Acetaldehyde	-9.726	-9.927	1.838	1.530
73	Ethoxy ethane	-9.413	-9.634	2.132	1.337
74	Formic acid	-10.823	-11.102	2.562	2.217
75	Hydrogen peroxide	-11.070	-11.238	2.784	2.246
76	Water	-12.096	-12.261	1.770	1.249
77	Carbon dioxide	-13.216	-13.429	4.248	1.448
78	Carbon disulfide	-9.590	-9.795	0.385	0.128
79	Carbon oxide sulfide	-10.821	-10.895	1.865	1.520
80	Carbon oxide selenide	-10.055	-10.397	1.466	1.198
81	Carbon monoxide	-13.866	-13.891	1.377	1.052
82	Ozone	-12.089	-12.478	-1.349	-1.726
83	Sulfur dioxide	-11.855	-12.049	-0.234	-0.573
84	Beryllium monoxide	-9.355	-9.465	-1.842	-1.990
85	Magnesium monoxide	-7.153	-7.206	-1.337	-1.544
86	Toluene	-8.565	-8.758	1.594	1.289
87	Ethylbenzene	-8.506	-8.677	1.707	1.307
88	Hexafluorobenzene	-9.560	-9.695	0.992	0.075
89	Phenol	-8.185	-8.489	1.539	1.261
90	Aniline	-7.633	-7.848	1.596	1.396
91	Pyridine	-9.378	-9.479	1.063	0.849
92	Guanine	-7.736	-7.913	1.247	0.806
93	Adenine	-8.013	-8.183	1.014	0.801
94	Cytosine	-8.337	-8.535	0.831	0.598
95	Thymine	-8.757	-8.946	0.683	0.418
96	Uracil	-9.130	-9.304	0.631	0.381
97	Urea	-9.507	-9.711	1.469	0.907
98	Silver dimer	-6.867	-7.013	-0.486	-0.663
99	Copper dimer	-7.471	-7.622	-0.477	-0.602
100	Copper cyanide	-10.130	-10.082	-0.945	-1.075

S4 GW5000 QP Energies

All values are also available in .CVS format

Table S5: G_0W_0 @PBE0 HOMO QP energies for 20 large from GW5000 (all values in eV). The numbers in the second column refer to the system numbers in the reference⁴ and the ordering of systems is the same as in the main text.

	Name	aug-DZP		TZ2P	
		Basic	Normal	Good	
1	53699	-5.839	-5.725	-5.790	-5.796
2	47797	-7.020	-6.993	-7.024	-7.024
3	47126	-6.861	-6.905	-6.914	-6.901
4	50280	-6.169	-6.184	-6.243	-6.241
5	48940	-7.316	-7.358	-7.378	-7.351
6	46250	-6.172	-6.062	-6.082	-6.135
7	45406	-6.522	-6.623	-6.599	-6.607
8	48237	-7.035	-7.047	-7.077	-7.095
9	44870	-8.035	-8.084	-8.084	-8.083
10	51751	-5.707	-5.837	-5.851	-5.848
11	47842	-6.579	-6.765	-6.767	-6.767
12	48180	-7.614	-7.722	-7.721	-7.720
13	44586	-6.048	-6.069	-6.073	-6.136
14	47776	-8.377	-8.618	-8.618	-8.617
15	49155	-6.374	-6.574	-6.569	-6.594
16	48578	-7.562	-7.651	-7.650	-7.649
17	47017	-7.252	-7.229	-7.152	-7.144
18	47010	-6.373	-6.547	-6.550	-6.562
19	48008	-7.186	-7.263	-7.252	-7.250
20	47960	-6.036	-5.896	-5.981	-5.983

Table S6: G_0W_0 @PBE0 LUMO QP energies for 20 large from GW5000 (all values in eV) for different threshold qualities (for TZ2P). The numbers in the second column refer to the system numbers in the reference⁴ and the ordering of systems is the same as in the main text.

	Name	aug-DZP		TZ2P	
		Basic	Normal	Good	
1	53699	-1.910	-1.797	-1.862	-1.872
2	47797	-0.493	-0.370	-0.379	-0.379
3	47126	-0.775	-0.658	-0.658	-0.657
4	50280	-0.804	-0.793	-0.795	-0.795
5	48940	-0.303	-0.255	-0.251	-0.251
6	46250	-0.691	-0.837	-0.640	-0.673
7	45406	-0.703	-0.607	-0.606	-0.606
8	48237	-0.057	-0.292	-0.153	-0.163
9	44870	0.119	0.127	0.127	0.127
10	51751	-0.189	-0.215	-0.144	-0.136
11	47842	0.017	-0.123	-0.125	-0.125
12	48180	-0.191	-0.133	-0.138	-0.138
13	44586	-0.492	-0.514	-0.513	-0.513
14	47776	0.180	0.117	0.116	0.116
15	49155	-0.284	-0.305	-0.347	-0.346
16	48578	0.287	0.269	0.269	0.269
17	47017	-1.803	-1.363	-1.498	-1.482
18	47010	0.271	0.171	0.183	0.184
19	48008	-0.475	-0.346	-0.341	-0.333
20	47960	-1.149	-1.127	-1.084	-1.077

Table S7: G_0W_0 @PBE0 HOMO and LUMO QP energies for 250 randomly selected systems from GW5000 (all values in eV) for different threshold qualities (for TZ2P). The numbers in the second column refer to the system numbers in the reference⁴ and the ordering of systems is the same as in the main text.

	Name	HOMO		LUMO	
		aug-DZP	TZ2P	aug-DZP	TZ2P
1	10214	-9.861	-10.006	-1.834	-1.944
2	11403	-10.740	-10.937	0.711	0.604
3	23303	-7.077	-7.261	-1.066	-1.232
4	37765	-8.934	-9.091	0.222	0.145
5	5760	-10.026	-10.543	0.145	-0.020
6	18255	-8.425	-8.570	-0.793	-0.841
7	21895	-8.903	-9.097	0.201	0.121
8	15634	-7.972	-8.162	0.451	0.388
9	12569	-9.043	-9.146	-0.011	-0.100
10	27595	-9.125	-9.285	-0.809	-0.885
11	10450	-7.374	-7.564	0.094	0.037
12	56782	-8.312	-8.510	0.027	-0.064
13	37128	-8.136	-8.348	-1.662	-1.838
14	25240	-9.216	-9.354	0.292	0.231
15	55516	-8.685	-8.858	-0.031	-0.089
16	54009	-7.426	-7.530	0.335	0.331
17	9202	-7.869	-8.073	-0.653	-0.806
18	22078	-6.960	-7.144	-1.100	-1.134
19	17502	-8.115	-8.266	-0.226	-0.302
20	1942	-7.509	-7.669	0.466	0.418
21	57610	-7.689	-7.844	0.398	0.374
22	2869	-8.306	-8.448	-0.618	-0.703
23	40494	-7.665	-7.827	-0.224	-0.289
24	60360	-8.312	-8.458	-0.189	-0.287
25	13505	-7.319	-7.417	-0.067	-0.098
26	59304	-9.199	-9.437	-1.126	-1.302
27	57383	-8.917	-9.130	-0.710	-0.862
28	55803	-8.678	-8.878	-0.507	-0.564
29	32571	-8.680	-8.879	0.200	0.181
30	4257	-7.909	-8.113	0.193	0.167
31	22407	-8.448	-8.592	-1.023	-1.093
32	33146	-8.693	-8.854	0.270	0.187
33	4465	-7.682	-7.779	-0.226	-0.252
34	3387	-7.360	-7.458	-0.335	-0.399
35	1761	-7.816	-7.961	0.120	0.041
36	7474	-7.871	-8.051	-0.266	-0.347
37	60545	-7.566	-7.687	0.031	-0.023
38	56584	-9.642	-9.767	-0.809	-0.909
39	55110	-8.095	-8.217	0.282	0.221
40	53842	-7.954	-8.042	-0.781	-0.810
41	60749	-7.468	-7.619	-0.637	-0.687
42	58846	-7.789	-7.951	0.162	0.094
43	10698	-9.038	-9.184	-0.435	-0.456
44	389	-8.086	-8.201	-0.178	-0.158
45	55259	-7.354	-7.482	-0.507	-0.587
46	57147	-6.917	-7.026	-0.214	-0.289
47	6527	-8.345	-8.420	-0.878	-0.922
48	54908	-6.809	-6.990	-1.443	-1.525
49	6838	-8.484	-8.615	0.258	0.224
50	46362	-8.312	-8.474	0.350	0.277
51	48399	-7.424	-7.579	-0.774	-0.829
52	61346	-7.545	-7.685	0.158	0.123
53	2686	-7.462	-7.621	-0.997	-1.067

Continued on next page

	Name	HOMO		LUMO	
		aug-DZP	TZ2P	aug-DZP	TZ2P
54	60181	-7.597	-7.784	-0.609	-0.661
55	6247	-7.542	-7.673	0.220	0.160
56	38315	-8.282	-8.424	-0.255	-0.321
57	33531	-7.203	-7.369	-0.156	-0.210
58	16444	-7.931	-8.148	-0.395	-0.476
59	10978	-6.983	-7.113	0.222	0.178
60	59849	-8.296	-8.534	0.165	0.119
61	12919	-7.256	-7.435	-0.022	-0.086
62	48653	-7.273	-7.404	-1.096	-1.179
63	4002	-7.708	-7.870	-1.808	-1.902
64	31853	-7.484	-7.623	-0.546	-0.609
65	25789	-8.381	-8.506	0.068	0.030
66	13712	-7.521	-7.654	-0.637	-0.727
67	21105	-7.866	-8.009	-1.764	-1.860
68	40764	-8.239	-8.346	-1.573	-1.632
69	56219	-8.425	-8.592	-0.437	-0.493
70	56050	-8.389	-8.579	0.335	0.285
71	45218	-7.913	-7.973	-0.105	-0.165
72	23028	-8.367	-8.546	-0.147	-0.235
73	14226	-7.317	-7.483	0.199	0.143
74	7729	-8.470	-8.595	-0.471	-0.543
75	54412	-8.211	-8.433	-0.651	-0.749
76	59631	-7.101	-7.249	-0.358	-0.437
77	19910	-9.251	-9.407	-0.854	-0.920
78	15429	-6.181	-6.355	-0.425	-0.483
79	28162	-6.974	-7.206	0.151	0.079
80	8509	-8.713	-8.847	0.022	-0.063
81	56406	-7.024	-7.174	-0.334	-0.387
82	54233	-7.399	-7.523	0.339	0.308
83	41377	-7.968	-8.135	-0.020	-0.068
84	23853	-7.182	-7.335	0.054	-0.006
85	21611	-6.323	-6.450	-0.365	-0.393
86	60961	-7.611	-7.777	-0.825	-0.879
87	58206	-6.707	-6.803	-0.498	-0.536
88	24031	-5.993	-6.174	0.023	-0.050
89	1627	-7.198	-7.367	-1.077	-1.217
90	16	-6.928	-7.094	0.337	0.296
91	584	-10.062	-10.224	-1.184	-1.295
92	39917	-7.507	-7.710	0.342	0.272
93	39685	-7.540	-7.712	-0.573	-0.672
94	26685	-7.586	-7.734	-0.290	-0.333
95	22875	-7.158	-7.342	0.311	0.254
96	964	-7.808	-8.013	-0.114	-0.168
97	58653	-8.841	-8.947	0.122	0.008
98	26821	-7.647	-7.835	0.000	-0.028
99	18460	-6.755	-6.904	-0.617	-0.667
100	23652	-7.581	-7.792	0.102	-0.071
101	25412	-7.473	-7.715	-0.322	-0.385
102	21210	-7.677	-7.848	0.030	-0.036
103	25995	-7.012	-7.124	0.115	0.065
104	212	-7.697	-7.860	-0.208	-0.258
105	59124	-6.851	-7.021	-0.616	-1.054
106	27801	-7.611	-7.717	0.181	0.147
107	53566	-9.270	-9.509	0.679	0.587
108	45995	-7.406	-7.606	-0.072	-0.193
109	21361	-8.067	-8.185	-1.063	-1.117
110	1145	-7.097	-7.242	-0.387	-0.429
111	54680	-6.957	-7.115	0.197	0.092
112	28450	-7.101	-7.263	-0.651	-0.683

Continued on next page

	Name	HOMO		LUMO	
		aug-DZP	TZ2P	aug-DZP	TZ2P
113	16704	-5.880	-6.167	-0.812	-0.871
114	58443	-8.475	-8.668	0.447	0.347
115	3793	-8.475	-8.622	0.145	0.141
116	26458	-7.307	-7.474	0.183	0.120
117	20821	-7.881	-8.063	-0.640	-0.718
118	20649	-7.447	-7.584	0.390	0.314
119	57896	-7.321	-7.394	-0.314	-0.393
120	27000	-7.278	-7.337	0.126	0.094
121	24951	-7.149	-7.304	-0.119	-0.151
122	20065	-7.660	-7.808	-0.355	-0.427
123	35442	-6.787	-6.892	-0.473	-0.471
124	38639	-6.204	-6.352	0.059	0.011
125	24201	-6.454	-6.602	0.298	0.267
126	20311	-8.335	-8.508	0.270	0.260
127	19347	-8.017	-8.218	-1.483	-1.564
128	18611	-8.179	-8.375	0.477	0.361
129	1304	-8.403	-8.479	-1.140	-1.177
130	2403	-6.949	-7.035	-0.448	-0.522
131	19664	-8.339	-8.503	-0.571	-0.587
132	61133	-7.001	-7.153	0.033	-0.037
133	48162	-7.819	-7.938	-0.701	-0.736
134	27374	-7.595	-7.741	0.223	0.194
135	18825	-7.021	-7.133	-0.364	-0.399
136	19062	-7.293	-7.461	0.202	0.105
137	47200	-6.802	-6.979	-0.200	-0.241
138	3133	-10.356	-10.544	-1.231	-1.354
139	26246	-7.579	-7.784	-0.421	-0.539
140	24722	-6.758	-7.044	0.280	-0.011
141	24419	-8.315	-8.426	0.289	0.290
142	2142	-7.871	-7.985	-0.430	-0.475
143	1415	-7.555	-7.733	0.417	0.380
144	9040	-6.694	-6.832	0.309	0.297
145	30647	-7.499	-7.646	0.106	0.083
146	29484	-7.657	-7.799	-0.237	-0.308
147	28674	-7.811	-8.018	0.210	0.173
148	50401	-7.342	-7.635	0.310	0.225
149	16245	-7.276	-7.424	0.227	0.186
150	12004	-7.049	-7.356	0.035	-0.078
151	14979	-8.341	-8.596	0.391	0.313
152	8314	-8.666	-8.817	0.430	0.390
153	13321	-7.654	-7.828	-0.867	-0.921
154	5330	-8.041	-8.212	-0.128	-0.205
155	30510	-6.565	-6.589	-0.052	-0.040
156	12143	-8.016	-8.180	-0.353	-0.437
157	7902	-7.937	-7.989	-0.013	0.003
158	7348	-7.844	-8.021	0.265	0.265
159	4727	-7.459	-7.633	0.374	0.265
160	45485	-7.783	-7.883	-1.034	-1.066
161	30240	-6.984	-6.982	0.265	0.253
162	29288	-8.967	-9.193	0.278	0.183
163	5948	-6.558	-6.674	0.186	0.173
164	14670	-7.744	-7.898	-0.385	-0.381
165	12405	-7.611	-7.782	0.014	-0.028
166	8115	-7.624	-7.807	-0.420	-0.444
167	22699	-7.751	-8.181	-1.044	-1.095
168	13736	-6.935	-7.027	0.028	0.046
169	9844	-8.092	-8.268	0.049	0.019
170	8740	-7.723	-7.841	0.073	0.101
171	46991	-8.445	-8.586	-0.339	-0.390

Continued on next page

	Name	HOMO		LUMO	
		aug-DZP	TZ2P	aug-DZP	TZ2P
172	30014	-6.665	-6.786	-0.843	-0.860
173	28006	-7.303	-7.427	-0.231	-0.235
174	16849	-7.541	-7.693	0.065	0.007
175	30833	-7.397	-7.517	-0.540	-0.616
176	13722	-7.551	-7.710	-0.140	-0.193
177	4986	-8.325	-8.469	0.196	0.276
178	31114	-7.323	-7.491	-0.103	-0.159
179	29738	-7.666	-7.778	0.292	0.275
180	15938	-7.645	-7.784	0.021	0.007
181	31332	-7.543	-7.686	-0.123	-0.166
182	9538	-8.261	-8.320	-1.122	-1.133
183	5179	-7.012	-7.116	-0.740	-0.738
184	28988	-7.242	-7.501	0.034	-0.078
185	14098	-6.731	-6.865	-0.217	-0.263
186	52978	-8.001	-8.096	0.675	0.590
187	13151	-7.525	-7.712	0.208	0.137
188	35225	-7.648	-7.882	0.436	0.299
189	31529	-7.470	-7.636	0.327	0.301
190	13702	-6.510	-6.649	0.427	0.440
191	7071	-7.105	-7.254	-0.017	-0.075
192	47575	-7.469	-7.615	-0.454	-0.450
193	15273	-7.085	-7.261	0.163	0.086
194	13760	-7.038	-7.082	-0.146	-0.132
195	11661	-8.027	-8.226	0.330	0.283
196	11151	-7.744	-7.844	-0.402	-0.447
197	42090	-7.331	-7.487	0.026	-0.040
198	38920	-6.739	-6.840	-0.697	-0.634
199	36205	-8.119	-8.277	-0.583	-0.622
200	32294	-6.457	-6.550	-1.260	-1.284
201	18111	-6.820	-6.925	-0.024	-0.063
202	42908	-6.885	-7.107	-0.035	-0.149
203	51981	-8.108	-8.233	-0.143	-0.135
204	40978	-8.508	-8.649	0.492	0.572
205	49946	-7.363	-7.598	-0.086	-0.164
206	44205	-7.460	-7.071	-0.606	-0.212
207	43090	-6.498	-6.596	-0.758	-0.787
208	40143	-7.710	-7.844	-0.574	-0.578
209	49106	-7.441	-7.580	-0.552	-0.572
210	34005	-7.253	-7.336	-0.045	-0.017
211	39175	-6.431	-6.552	0.057	0.040
212	36515	-7.551	-7.698	-0.180	-0.239
213	43905	-7.235	-7.392	0.080	0.039
214	34913	-6.783	-6.961	-0.113	-0.173
215	37381	-7.796	-8.050	0.459	0.359
216	51317	-6.743	-6.889	-0.284	-0.317
217	43385	-7.059	-7.233	-0.349	-0.393
218	42754	-6.852	-7.027	-0.246	-0.363
219	41897	-7.510	-7.653	-0.400	-0.616
220	39418	-7.737	-7.875	-0.556	-0.574
221	33692	-8.145	-8.312	-0.282	-0.331
222	53229	-8.268	-8.427	-0.081	-0.069
223	43634	-7.465	-7.643	0.016	-0.114
224	41571	-6.212	-6.399	-0.406	-0.501
225	17264	-7.013	-7.084	-0.680	-0.698
226	42424	-7.600	-7.755	0.385	0.326
227	17807	-7.216	-7.358	0.146	0.103
228	35790	-7.028	-7.096	-0.123	-0.073
229	52590	-6.456	-6.417	-0.433	-0.611
230	36735	-6.913	-7.126	-0.899	-1.041

Continued on next page

	Name	HOMO		LUMO	
		aug-DZP	TZ2P	aug-DZP	TZ2P
231	34307	−7.269	−7.425	−0.919	−0.915
232	33372	−7.157	−7.421	0.383	0.239
233	32947	−6.888	−7.021	−0.542	−0.579
234	38018	−6.897	−7.060	−0.063	−0.079
235	34564	−6.437	−6.467	−0.253	−0.318
236	16982	−7.388	−7.630	0.032	−0.058
237	51045	−7.286	−7.415	0.256	0.248
238	51639	−7.426	−7.573	−0.803	−0.879
239	48947	−6.835	−6.850	0.108	0.159
240	46610	−8.042	−8.316	0.220	0.066
241	45666	−8.281	−8.487	0.327	0.232
242	46821	−6.772	−6.926	−0.570	−0.621
243	52259	−7.938	−8.132	−0.358	−0.368
244	50771	−7.554	−7.693	0.115	0.153
245	49471	−6.039	−6.103	−1.372	−1.402
246	50224	−8.174	−8.341	−0.239	−0.231
247	47960	−5.915	−5.982	−1.035	−1.077
248	44870	−7.972	−8.083	0.128	0.127
249	44586	−6.048	−6.127	−0.492	−0.512
250	47797	−6.961	−7.024	−0.445	−0.379

Table S8: Parameters of the linear fits $f(x) = a \times x + b$ shown in figure 8 in the main text. All value are in eV.

basis set	HOMO		LUMO		gap	
	a	b	a	b	a	b
aug-DZP	−0.000 431	0.653 289	−0.000 734	0.814 004	−0.000 303	0.160 719
TZ2P	−0.000 285	0.482 206	−0.000 524	0.731 793	−0.000 239	0.249 591
def-TZVP	−0.000 136	0.400 648	−0.000 365	0.515 398	−0.000 229	0.114 750
def-QZVP	−0.000 126	0.190 429	−0.000 247	0.245 059	−0.000 121	0.054 630

S5 Numerical frequency integration

All pretabulated grid points and integration weights (the latter are needed for RPA correlation energies) used in our work to obtain converged imaginary frequency grids are available as .txt-file. For all tabulated ranges, the file also includes the L_2 -norm of the minimized error-distribution function⁵ for all ranges of transition energies $[1, \epsilon_{max}/\epsilon_{min}]$, where ϵ_{min} (ϵ_{max}) denotes the smallest (largest) KS orbital energy difference.

$$\|\eta(x; \{\gamma_i, \omega_i\})\|_2 = \left\| \frac{1}{x} - \frac{1}{\pi} \sum_{i=1}^{N_\omega} \gamma_i \left(\frac{2x}{x^2 + \omega_i^2} \right)^2 \right\|_2; \quad x \in [1, \epsilon_{max}/\epsilon_{min}]. \quad (7)$$

References

- (1) Gao, W.; Chelikowsky, J. R. Real-Space Based Benchmark of G0W0 Calculations on GW100: Effects of Semicore Orbitals and Orbital Reordering. *J. Chem. Theory Comput.* **2019**, *15*, 5299–5307.
- (2) Förster, A.; Franchini, M.; van Lenthe, E.; Visscher, L. A Quadratic Pair Atomic Resolution of the Identity Based SOS-AO-MP2 Algorithm Using Slater Type Orbitals. *J. Chem. Theory Comput.* **2020**, *16*, 875–891.
- (3) Jackson, J. D. *Classical electrodynamics*; AAPT, 1999.
- (4) Stuke, A.; Kunkel, C.; Golze, D.; Todorović, M.; Margraf, J. T.; Reuter, K.; Rinke, P.; Oberhofer, H. Atomic structures and orbital energies of 61,489 crystal-forming organic molecules. *Sci. Data* **2020**, *7*, 1–11.
- (5) Kaltak, M.; Klimeš, J.; Kresse, G. Low scaling algorithms for the random phase approximation: Imaginary time and laplace transformations. *J. Chem. Theory Comput.* **2014**, *10*, 2498–2507.

Graphical TOC Entry

